Extensive, water-rich magma reservoir beneath southern Montserrat

M. Edmonds[1]*, S. C. Kohn[2], E. H. Hauri[3], M. C. S. Humphreys[4], M. Cassidy[5]

1 Department of Earth Sciences, Downing Street, Cambridge, CB2 3EQ, UK
2 Department of Earth Sciences, Wills Memorial Building, Queen's Road, Bristol, UK
3 Carnegie Institute of Washington, 5241 Broad Branch Rd, NW Washington, DC 20015, USA
4 Department of Earth Sciences, Durham University, Science Labs, Durham DH1 3LE, UK
5 Institute for Geosciences, Johannes Gutenberg University of Mainz, Mainz, 55128, Germany

** Corresponding author; me201@cam.ac.uk*

Abstract

South Soufriere Hills and Soufriere Hills volcanoes are two km apart at the southern end of the island of Montserrat, West Indies. Their magmas are distinct geochemically, despite these volcanoes having been active contemporaneously at 131-129 ka. We use the water content of pyroxenes and melt inclusion data to reconstruct the bulk water contents of magmas and their depth of storage prior to eruption. Pyroxenes contain up to 281 ppm H_2O, with significant variability between crystals and from core to rim in individual crystals. The Al content of the enstatites from Soufriere Hills Volcano (SHV) is used to constrain melt-pyroxene partitioning for H_2O. The SHV enstatite cores record melt water contents of 6-9 wt%. Pyroxene and melt inclusion water concentration pairs from South Soufriere Hills basalts independently constrain pyroxene-melt partitioning of water and produces a comparable range in melt water concentrations. Melt inclusions recorded in plagioclase and in pyroxene contain up to 6.3 wt% H_2O. When combined with realistic melt CO_2 contents, the depth of magma storage for both volcanoes ranges from 5 to 16 km. The data are consistent with a vertically protracted crystal mush in the upper crust beneath the southern part of Montserrat which contains heterogeneous bodies of eruptible magma. The high water contents of the magmas suggest that they contain a high proportion of exsolved fluids, which has implications for the rheology of the mush and timescales for mush reorganisation prior to eruption. A depletion in water in the outer 50-100 microns of a subset of pyroxenes from pumices from a Vulcanian explosion at Soufriere Hills in 2003 is consistent with diffusive loss of hydrogen during magma ascent over 5-13 hours. These timescales are similar to the mean time periods between explosions in 1997 and in 2003, raising the possibility that the driving force for this repetitive explosive behaviour lies not in the shallow system, but in the deeper parts of a vertically protracted crustal magma storage system.

1. Introduction

Quantifying the water budget of arc magmas is critical for the investigation of a large range of research problems associated with subduction zones, including understanding how subduction cycling of volatiles works (Rüpke et al., 2004), arc magma petrogenesis (Baker et al., 1994; Gaetani et al., 1993; Grove and Kinzler, 1986), assimilation of crustal melts (Annen et al., 2006; Petford and Gallagher, 2001), oxidation state (Evans et al., 2012; Stamper et al., 2014), melt buoyancy (Spera, 1984), melt rheological properties (Cashman and Blundy, 2000), the role of aqueous fluids in transporting metals (Williams-Jones and Heinrich, 2005) and ultimately, the style of magma eruption at the surface (Castro and Dingwell, 2009; Roggensack et al., 1997). Ascending water-rich primitive magmas in arcs may stall where their buoyancy prohibits further ascent (Plank et al., 2013) or where they underplate larger volumes of evolved crystal-rich magmas (Bachmann and Bergantz, 2006; Couch et al., 2001) or large trans-crustal mush zones (Bergantz et al., 2015; Cashman and Blundy, 2013; Christopher et al., 2015; Ruprecht et al., 2012) that may be held at sub-solidus temperatures for long timescales (10^4-10^5 years) (Cooper and Kent, 2014) before being remobilised by magma recharge (Bachmann and Bergantz, 2006; Bergantz et al., 2015; Burgisser and Bergantz, 2011).

The emerging view is that these crystal-rich, intermediate magma reservoirs are vertically protracted (extending down to the mid-crust), consisting of melt-rich lenses, crystal-rich mush (Cashman and Blundy, 2013; Cashman and Sparks, 2013; Cooper and Kent, 2014; Humphreys et al., 2006) and perhaps, in the shallow crust, fluid-rich regions (Christopher et al., 2015). Andesites may be assembled by processes that might involve destabilisation, overturn and mixing of such “layers” on short timescales (years) prior to eruptions (Bergantz et al., 2015; Burgisser and Bergantz, 2011), perhaps aided by partial melting at vapor-saturated conditions (Huber et al., 2011). The physical location of such regions of magma storage, from which magmas are extracted prior to eruption and the timescales on which this occurs, are not fully understood. Where vapor saturation occurs in these protracted magma reservoirs is critical for understanding mush reactivation and magma mixing, as the presence or generation of an exsolved fluid phase increases overpressure and generates mechanical energy. The presence of an exsolved gas phase also allows physical processes such as gas-driven filter pressing to take place (Pistone et al., 2015; Sisson and Bacon, 1999), which might be important for the generation of crystal-poor regions of the melt in the mush. There are also geochemical implications of an exsolved water-rich fluid: once an exsolved gas phase is present, partitioning of other volatile elements may take place, such as sulfur and chlorine (Scaillet et al., 1998; Wallace and Edmonds, 2011) as well as metals that have an affinity for a hydrous vapor phase (Zajacz and Halter, 2009).

Unravelling the petrological record in erupted volcanic rocks to understand melt volatile contents and the architecture of pre-eruptive magma reservoirs is challenging. Traditionally melt inclusions have been the mainstay of such studies (Blundy and Cashman, 2008; Cervantes and Wallace, 2003; Walker et al., 2003), in combination with geobarometers e.g. clinopyroxene-melt equilibria (Putirka et al., 1996), aluminium in hornblende (Ridolfi et al., 2010) and plagioclase-liquid hygrometers (Lange et al., 2009). Melt inclusions record "snapshots" of melt trapped at intervals through melt differentiation (Kent and Elliott, 2002; Lowenstern, 1995; Métrich and Wallace, 2008). Very often however, the pressures obtained from CO_2-H_2O in melt inclusions are considerably lower than those obtained using crystal-melt equilibria (Neave et al., 2013) and this is ascribed to trapping during magma ascent (Blundy and Cashman, 2005) melt inclusion leakage or CO_2 loss into a shrinkage bubble (Esposito et al., 2014; Hartley et al., 2014; Moore et al., 2015; Sides et al., 2014; Steele-Macinnis et al., 2011; Wallace et al., 2015). The melt inclusion record may be inherently biased as melts are preferentially trapped immediately after periods of rapid crystal growth (Faure and Schiano, 2005) or, in the case of plagioclase, during periods of heating, dissolution and reprecipitation (Nakamura and Shimakita, 1998). They may be sealed off during periods of magma ascent and degassing at low crustal pressures (Blundy and Cashman, 2005). The melt inclusions are sometimes not faithful recorders of original trapped compositions: it has been shown that hydrogen diffuses out of olivine-hosted melt inclusions extremely rapidly at low pressures (where a concentration gradient is established due to the degassing of the carrier liquid) and high temperatures (Gaetani et al., 2012) and similar high rates of diffusion are likely through the other crystal phases.

Nominally anhydrous minerals such as pyroxene may hold trace amounts of water in their structure, up to a few hundred ppm (Bell and Rossman, 1992; Grant et al., 2007a; Hauri et al., 2006; Kohn and Grant, 2006) and this may be a promising complementary tool to use alongside melt inclusion analysis of water. Erupted crustal magmatic pyroxenes ought to preserve a record of melt water contents if such a record is not erased or homogenized by diffusive processes. This record may be deciphered if the partitioning behaviour of water between melt and pyroxene is understood. Previous work has used the hydrogen content of clinopyroxenes and the water content of coexisting melt inclusions in basalts to show that pyroxenes have potential to record both isobaric crystallization and decompression degassing in their zoning profiles, which are not modified by diffusive processes on typical timescales of eruption (O'Leary et al., 2010; Wade et al., 2008; Weis et al., 2015). In this study we extract a record of hydrogen and major element concentrations in volcanic orthopyroxenes in andesite erupted during a Vulcanian explosion from Soufrière Hills Volcano, Montserrat; and in

clinopyroxenes erupted in hybrid basalts from the neighbouring volcano, South Soufriere Hills (Cassidy et al., 2015a). This crystal record is used to infer melt water contents using our established understanding of hydrogen partitioning between melt and orthopyroxene (Aubaud et al., 2004; Dobson et al., 1995; Grant et al., 2006, 2007b; Hauri et al., 2006; Koga et al., 2003; Rosenthal et al., 2015; Tenner et al., 2009), as well as observations of water partitioning between clinopyroxene and melt inclusions (O'Leary et al., 2010; Wade et al., 2008). The estimated melt water contents derived from the pyroxene records are used to infer magma storage pressures, assuming the melts are vapour-saturated and taking into account the lowered activity of water in the melts due to the presence of dissolved CO_2. The saturation pressures derived from the pyroxenes are compared to those derived from the melt inclusion records and clinopyroxene-liquid barometry for lavas from South Soufrière Hills volcanoes. We evaluate how the water profiles in the enstatites from Soufriere Hills may have been modified by diffusive loss of water during magma ascent and degassing of the carrier liquid. The potential of large pyroxenes in relatively cool magmas for preserving detailed records of deep magma storage in the arc crust is assessed, along with the implications for understanding the architecture of magma storage beneath the southern part of the island of Montserrat and for the transcrustal mush paradigm.

2. Geological setting

This contribution focusses on the magmatic system connected to the Soufrière Hills and South Soufriere Volcanoes (SHV and SSH), Montserrat, West Indies, where many studies have laid the groundwork for understanding magma storage and transport. The island of Montserrat is located in the northern part of the Lesser Antilles; a 750 km long chain of volcanic islands formed as a result of the slow (2 cm yr^{-1}) subduction of the North American plate beneath the Caribbean plate (**figure 1**). Montserrat lies on crust that is ~ 30 km thick (Sevilla et al., 2010). The island comprises four volcanic centres: Silver Hills (2600-1200 ka), Centre Hills (950-550 ka), Soufriere Hills (282 ka to present) and South Soufriere Hills (131 to 128 ka) (Harford et al., 2002).

The Soufrière Hills Volcano erupted crystal-rich andesite magma between November 1995 and February 2010 (Wadge et al., 2014). The andesite is comprised of ~ 40 vol% macrocrysts (plagioclase, hornblende, orthopyroxene, magnetite, ilmenite and minor rounded quartz) in a groundmass of rhyolitic glass (with 72-75 wt% SiO_2) and a microcryst assemblage similar to the macrocrysts, with the addition of minor clinopyroxene (Humphreys et al., 2009b; Murphy et al., 2000). The andesite contains mafic enclaves with basaltic to basaltic andesite composition and macrocrysts inherited from the andesite (Plail et al., 2014). The enclaves exhibit compositions and features suggestive of hybridisation between basalt and andesite before

148 enclave formation, typical of enclaves observed elsewhere (Bacon, 1986; Plail et al., 2014;
149 Ruprecht et al., 2012). Dome lavas are highly crystalline; pumices erupted during Vulcanian
150 explosive activity have a range of vesicularities reflecting their position in the eruptive conduit
151 (Giachetti et al., 2010). Sequences of Vulcanian explosions (with durations of a few minutes) in
152 1997 and 2003 took place quasi-periodically with inter-explosion repose periods of hours to
153 days (Druitt et al., 2002; Edmonds et al., 2006). Based on microlite textures in the pumice, it
154 has been suggested that the Vulcanian explosions evacuated 1-2 km of conduit and occurred
155 concurrent with the breaching of a dense, degassed plug at the top of the conduit (Clarke et
156 al., 2007). Numerical models, however, suggest that high and cyclic magma discharge rates,
157 which generate Vulcanian explosions, may be generated when magma reservoir pressures
158 increase to some critical level, owing to the non-linear rheological properties of the magma
159 (Melnik and Sparks, 2002), implying that the explosions are driven by some process at depth
160 and not by overpressures generated beneath a conduit-top plug.
161
162 It has been proposed, on the basis of ground deformation measured by GPS over fifteen years
163 of eruption, that a dual magma reservoir system exists beneath the island, with loci of magma
164 storage at 5-7 km and 10-12 km (Elsworth et al., 2008; Hautmann et al., 2010; Melnik and
165 Costa, 2014), but the observations are also consistent with a continuum of disseminated, small
166 magma storage areas distributed through the mid- and upper crust as recently proposed on
167 the basis of observed decoupled magma and gas fluxes (Christopher et al., 2015). A large-
168 scale seismic experiment failed to observe features consistent with a shallow magma reservoir
169 system at depths of < 5 km (Paulatto et al., 2010; Shalev et al., 2010), suggesting that either
170 melt exists in extremely low melt fractions and/or that the bulk of the magma storage is deeper
171 than 5 km. Magma ascent timescales for dome lavas have been estimated to be 1-3 weeks
172 during effusive volcanic activity (lava dome building) based on diffusion profiles in Fe-Ti oxides
173 that have been perturbed by heating (during mafic underplating) prior to eruption (Devine et al.,
174 2003).
175
176 South Soufriere Hills Volcano (at the far southern end of the island; **figure 1**) erupted basalts
177 and andesites containing plagioclase, olivine (with a composition of 62-84 mol% forsterite),
178 clinopyroxene, and titanomagnetite (Cassidy et al., 2015a). Recent work has shown that South
179 Soufriere Hills magmas have distinct trace element and Pb isotopic signatures of those from
180 neighbouring Soufriere Hills, suggesting considerable and prolonged heterogeneity in the
181 magma reservoir system beneath the southern part of the island (Cassidy et al., 2012). The
182 basalts, like the andesites from Soufriere Hills, are extensively hybridised, showing signs of
183 recharge and disequilibrium. The glasses are considerably more evolved than the whole rock
184 composition, consistent with an origin by mixing between evolved liquids and mafic crystal

mush phases (Cassidy et al., 2015a). It has been proposed that the more mafic whole rock composition over the SHV andesites reflects the tapping a deeper part of the transcrustal mush owing to the extensional tectonic regime across the southern part of the island (Cassidy et al., 2015a).

3. Methods

3.1. Samples

Samples are pumices erupted during Vulcanian explosions that occurred in July 2003 with densities of 800-1200 kgm^{-3} (Edmonds et al., 2006). The bulk composition of the pumice is andesite, but it is comprised of rhyolitic glass with phenocrysts of amphibole, plagioclase and orthopyroxene making up 40 vol% (Murphy et al., 2000). Pumices were crushed and the enstatites picked in the size fraction 2-5 mm. Pyroxenes are black in hand specimen, with euhedral crystal shapes (**figure 2**), elongated parallel to the c direction. In thin section they are pale brown and weakly pleochroic, with straight extinction and mid to low first-order birefringence colors. The enstatites contained abundant magnetite and ilmenite inclusions but only very few melt inclusions and most were < 10 microns across.

Samples from South Soufriere Hills volcano are fragments of basaltic tephra erupted ~ 130 ka (Cassidy et al., 2015a). The samples contain olivine (cores up to 84 mol% Fo), clinopyroxene, plagioclase (cores up to 92 mol% An) and titanomagnetite making up ~40 vol% macrocrysts. Clinopyroxenes are black in hand specimen and pleochroic in brown-green in thin section. They contained melt inclusions up to 100 microns in maximum dimension.

The pyroxenes were mounted in crystal bond and polished on one side, before being mounted in indium metal to eliminate background contamination by hydrogen outgassing from epoxy. The indium mounts were gold-coated prior to SIMS analysis. After SIMS, the gold coat was polished off and replaced with a carbon coat for electron probe microanalysis (EPMA).

3.2. Secondary Ion Microscopy (SIMS)

The abundance of H_2O in glass inclusions and in orthopyroxene was analysed using Secondary Ion Microscopy (SIMS) at the NERC Ion Probe facility in Edinburgh and at the SIMS Lab, Carnegie Institution, Washington D.C. For the analysis of melt inclusions at the NERC ion probe facility, a 5nA O^- ion beam on a pre-rastered spot of 10 microns in size was used. Counts were collected over 10 cycles. H_2O contents were calculated from a daily calibration plot of H/Si vs. H_2O, which gives a straight line with R^2 0.97 or better (**figure 3B**) for a set of well-characterised standard glasses. At the Carnegie Institution SIMS lab a Cameca 6f ion probe and a Cs^+ beam was used. During the pre-analysis rastering of a 40 x 40 micron

spot, secondary ion images of ^{1}H, ^{12}C and ^{35}Cl were projected on the channel plate, which helped to avoid inclusions and cracks, which appear as bright features on the projected image. The Cs^{+} beam generates the negatively charged secondary ions $^{1}H^{-}$ and $^{30}Si^{-}$ (the internal standard) and a linear calibration using a set of standard glasses was used to calculate H_2O contents (**figure 3A**) (Hauri, 2002).

The abundance of H^{+} in pyroxene was quantified using methods developed for the microanalysis of trace amounts of hydrogen (Koga et al., 2003). Using the Carnegie Institution Cameca 6f, pressure in the ion probe sample chamber was $<6 \times 10^{-10}$ Torr during all analyses. A primary beam 20 μm in diameter was rastered over a 50 μm x 50 μm area for 1 – 3 min prior to analysis. After each beam spot was carefully examined, the raster was stopped and a field aperture inserted to permit transmission of ions only from the central 8 μm of the 20 μm beam crater, thus avoiding transmission of hydrogen ions from the edge of the sputter crater and the surface of the sample. Counting times for ^{1}H and ^{30}Si were 5 and 10 s respectively. Detection limits for H_2O in pyroxene were typically 1–4 ppm H_2O, determined by the repeat analysis of synthetic H-free pyroxenes. Well-populated calibration curves for synthetic orthopyroxene crystals (with OH^{-} and H_2O concentrations measured by FTIR; Koga et al., 2003) for H_2O were used (**figure 3C**) (Hauri et al., 2006). Calibrations for H_2O were verified for glasses and minerals prior to each analytical session.

To analyse hydrogen in pyroxenes using the Cameca IMS-4F ion microprobe at the NERC ion probe facility at the University of Edinburgh, an O- primary beam was used with a net energy of ~17 KeV and a 20 μm spot diameter. Positive secondary ions were extracted and accelerated to ~4.5 KeV. A set of pyroxene profiles previously analysed using the Carnegie Institution Cameca 6f and by FTIR (see below) were analysed again (re-occupying the same spots) as knowns using the 4f, along with a set of NIST glasses. The linear calibration for H_2O provided by the NIST glasses (**figure 3B**) was used, along with a correction factor from the comparison between the 6f and 4f pyroxene analyses (which was equal to 1.763) to obtain the H_2O concentration of the pyroxene unknowns. Repeat analysis of pyroxene spots and a nominally anhydrous olivine in each analytical session indicates a consistent precision of better than 10% and a detection limit of 2-4 ppm H_2O.

3.3. Electron probe microanalysis

Mineral and glass major element and S, Cl and F compositions were analysed using a Cameca SX-100 electron microprobe at the University of Cambridge. Pyroxene major element composition was analysed with a 15 kV, 10 nA beam focused to a 2 μm spot. Counting times

were 300 seconds. A large TAP crystal was used to improve detection limits. Detection limits for Al ranged from 90 to 256 ppm. Glasses were analysed using a 15 μm, 15 kV beam with 2-4 nA beam current for major elements and 10 nA beam for minor elements. Na and Si were analysed first with short counting times in order to reduce migration of alkalis (Blundy and Cashman, 2005; Devine et al., 1995; Humphreys et al., 2006).

4. Results

We have made 247 point SIMS measurements of 34 enstatite crystals in andesites from Soufrière Hills Volcano, Montserrat and 12 pyroxenes (enstatites and augites) in basalts from South Soufriere Hills Volcano.

4.1 Orthopyroxenes from Soufriere Hills Volcano andesites

The major element composition of the orthopyroxenes from SHV are presented in **Table 1** and in **figure 4**. Backscattered electron images show that some of the pyroxenes have a Mg-rich overgrowth of variable thickness at the crystal rims (**figure 3B, C**). The pyroxenes are enstatites, with composition $En_{57-61}Fs_{37-41}Wo_{1.8-2.2}$. Magnesium numbers (Mg#) for the enstatites range from 63.6 to 68.2 (**Table 1**). The concentrations of MgO, FeO_{tot} and SiO_2 are shown in **figure 4**. The Al_2O_3 content of the enstatites ranges from 0.4 to 1.2 wt% (**figure 4C, D**). There is no systematic relationship between the enstatite major element composition and distance from rim (**figure 4D**), indicating that compositional zoning, where present, is not simple.

The H_2O content of the enstatites, measured by SIMS, ranges up to 272 ppm and correlates with enstatite Al_2O_3 content (with r = 0.62) (**table 1**; **figure 5A**). H_2O content does not correlate with any other measured major or minor element (Ti, Cr, Fe, Mg, Si, Ni, Mn, K or Na; **Table 1**). In general the most magnesian enstatites have the lowest Al_2O_3 and H_2O contents (**figure 5A**). Molar Al/H correlates strongly with Al_2O_3, as expected, with the most magnesian enstatites having the lowest H/Al for a fixed Al_2O_3 content (**figure 5B**) and the most H_2O-rich enstatites the highest H/Al for a fixed Al_2O_3 content (**figure 5C**). These plots illustrate that, even though there is a strong correlation between H_2O and Al_2O_3 content of the enstatite, there is considerable variability in enstatite H_2O content for a fixed Al_2O_3 content, demonstrating that, if we assume that partitioning behaviour between pyroxene and melt is fixed at a constant Al_2O_3, there must be variability in the H_2O content of the melt in which the enstatite grew to produce a range in both molar H/Al and enstatite H_2O contents (**figure 5**).

Individual profiles across crystals show considerable variability in H_2O and/or molar H/Al within a single crystal (e.g. **figure 6**). A majority of the crystals show a decrease in H_2O content in the

293 outer 50-100 microns of the crystal (**figures 6, 7**), which might be due to diffusive loss of
294 hydrogen during magma ascent and degassing (Lloyd et al., 2013), discussed later.

295 *4.2 Pyroxenes from South Soufriere Hills Volcano basalts*
296 Orthopyroxenes from South Soufriere Hills magmas are enstatites of a restricted composition:
297 $En_{65-67}Fs_{31-32}Wo_{2.5-3.0}$ and their Al_2O_3 content ranges from 1.0-1.4 wt% (**Table 2**).
298 Clinopyroxenes are augites of composition $En_{42-44}Fs_{14.5-16}Wo_{40-43}$ and a Al_2O_3 content of 1.5 to
299 3 wt% (**Table 2**). The water content of the pyroxenes ranges from 2 to 281 ppm (**Table 3;**
300 **Figure 7, 8**). Some of the pyroxenes contained melt inclusions with a water content ranging
301 from 0 to 6.19 wt% (**Table 3**). A plot of the water content of the pyroxenes against the water
302 content of the melt inclusions yields a regression line (excluding the marked points) with a
303 mean pyroxene-melt partition coefficient for water of 0.003 (**Figure 8**). The marked points in
304 **figure 8** are excluded from the regression as it seems likely that the melt inclusions close to
305 zero inside water-rich pyroxenes lost water by inclusion rupture and leakage. Profiles across
306 the crystals were not undertaken for the SSH pyroxenes.

307

308 **5. Discussion**
309
310 *5.1. Zoning in enstatites from andesites, Soufriere Hills Volcano*
311 Although the crystals are relatively homogeneous with regard to Mg# (**table 1**), considerable
312 variability in both H_2O and Al_2O_3 contents and in molar H/Al exists from core to rims of the
313 crystals. **Figure 9** shows how such zoning may be interpreted. Given that the partition
314 coefficient for hydrogen partitioning between pyroxene and melt is proportional to enstatite
315 Al_2O_3 content (Grant et al., 2006; Hauri et al., 2006; Kohn and Grant, 2006), then zoning in
316 Al_2O_3 in the pyroxene, caused by fractionation or by magma mixing, is associated with
317 changes in partitioning behaviour of water. If the pyroxene grew in a vapor-saturated melt,
318 such that the H_2O concentration in the melt remained approximately constant during
319 fractionation, the H_2O content of the crystal would be zoned, following the distribution of Al_2O_3
320 (**figure 9A**). The H_2O/Al_2O_3 ratio, however, would remain constant. If, in another scenario, the
321 pyroxene was compositionally homogeneous with respect to Al_2O_3 (e.g. **figure 9B**) and thus
322 the partition coefficient for hydrogen remained constant throughout crystal growth, one might
323 expect any zoning with respect to H_2O in the crystal to be due to variability in the melt H_2O
324 concentration during pyroxene growth, as illustrated in **figure 9B**, where the core of this crystal
325 grew in a more H_2O-rich melt than the rims. In this case the H_2O/Al_2O_3 ratio mirrors the trend in
326 pyroxene H_2O concentrations. The final example shown (**figure 9C**) is perhaps, inevitably,
327 closest to nature, whereby both the Al_2O_3 content of the pyroxene and also the H_2O content of

328 the melt surrounding the crystal varies, perhaps due to vapor-undersaturated fractionation,
329 progressive CO_2 fluxing (Métrich and Wallace, 2008) or magma mixing (Dixon et al., 1991), or
330 some combination of these processes. In this case the variation in H_2O concentrations through
331 the crystal will be controlled by both Al_2O_3 content and melt H_2O content. The trend in
332 H_2O/Al_2O_3 versus H_2O allows discrimination of these controls.

333 The data show that there is a correlation between Al_2O_3 and H_2O contents of the pyroxenes
334 (**figure 5A**), illustrating that a primary control on the H_2O content is Al_2O_3 content, which
335 controls the partition coefficient. There is considerable scatter however, as well as a negative
336 linear trend between H/Al and Al_2O_3 (**figure 5B**), which clearly indicates a dependence of
337 pyroxene H_2O content on melt H_2O content as well as a changing partition coefficient (**figure**
338 **9C**). Another way of stating this is that there is clearly a large range in H_2O contents for a
339 particular pyroxene Al_2O_3 content, which generates the range in H/Al ratios (**figure 5C**). These
340 observations suggest that real variability in melt H_2O content, as well as enstatite Al_2O_3
341 content, caused the H_2O zoning in the enstatites. These observations raise the possibility that
342 these crystals are preserving information on melt H_2O contents from deep in the crust prior to
343 magma ascent and eruption.
344
345 *5.2. Partitioning of H+ into pyroxenes from melt*
346 It has been shown that pure enstatite may hold up to 800 ppm water at 7.5 GPa and most
347 likely, pairs of protons attached to non-bridging oxygen atoms substitute for Mg^{2+} (Rauch and
348 Keppler, 2002). The solubility, and hence the partitioning of water into pyroxene, is enhanced
349 considerably however by the presence of aluminium in the crystal structure (Aubaud et al.,
350 2004; Hauri et al., 2006; Koga et al., 2003; Kohn and Grant, 2006; Mierdel and Keppler, 2004;
351 O'Leary et al., 2010; Rauch and Keppler, 2002; Stalder and Skogby, 2002; Stalder and
352 Skogby, 2003). The solubility of H_2O in pure enstatite has been observed to be dependent on
353 temperature at mantle pressures, although the temperature dependence becomes weak at low
354 pressures (<1000 MPa) (Mierdel and Keppler, 2004). Water solubility in enstatite increases
355 with pressure, reaching a maximum of ~1400 ppm at 8 GPa (Mierdel and Keppler, 2004). At a
356 pressure of 1 GPa, the solubility of H_2O in pure (Al-free) enstatite was found to be around 100
357 ppm (Mierdel and Keppler, 2004; Rauch and Keppler, 2002). The strongest control on water
358 solubility however, as discussed above, remains the Al content of the pyroxene; merely adding
359 1 wt% Al to enstatite triples the solubility of H_2O at 1500 MPa and 1100 °C (from 400 to 1200
360 ppm). It is proposed that this relationship can be extrapolated to both higher and lower
361 pressures (Rauch and Keppler, 2002), making the solubility for H_2O at pressures of <1000
362 MPa on the order of a few hundred ppm H_2O. At the pressures and temperatures of interest
363 here, we assert that H_2O remains well below the solubility limit for enstatite. The dominant

mechanism of hydroxyl incorporation into pyroxene is through solid solution of a Mg-Tschermaks component, $MgAl_2SiO_6$ (Grant et al., 2007a). Incorporation of H^+ is thought to take place via protonation of the oxygens which bridge the tetrahedral and octahedral sites (Kohn and Grant, 2006).

A synthesis of the existing experimental data for the partitioning of hydrogen into aluminium-bearing orthopyroxene is shown in **figure 10**, which includes experiments using pure water fluids (Aubaud et al., 2004; Grant et al., 2007a; Grant et al., 2006; Koga et al., 2003; Tenner et al., 2009) and those where the activity of water is less than unity (Hauri et al., 2006; Rosenthal et al., 2015). The data show that at lower water activities there may be a slight decrease in the partition coefficient of hydrogen for a particular pyroxene Al content, but further work is required to consolidate understanding of this behaviour, as there is clearly coupled variability in Al and water activity in the experiments of Rosenthal et al. (2015), making it difficult to deconvolve the effects of varying the water activity independently of Al. A regression through the pure water experiments yields the relation $D = 0.0031*X_{Al} + 0.0004$ (**figure 10**), which we use in the analysis below in the absence of a clear understanding of how the activity of water affects partitioning, if at all. This partition coefficient is identical to that obtained by regression through the South Soufriere Hills basalt pyroxene (both enstatite and augite plotted together) and melt inclusion water contents (**figure 8**).

5.3. Reconstruction of melt H_2O contents

A plot of Soufriere Hills (andesite) enstatite Al_2O_3 (converted to partition coefficient on the second axis) versus pyroxene H_2O content shows the data contoured for melt H_2O content, using the regression derived above (**figure 11**). The data suggest that the pyroxenes largely grew in melt with H_2O contents of between 6 and 9 wt% H_2O, with some data points reaching 4 and 10 wt%. Uncertainty on these estimates may be +/- 1 wt% and stems partly from the scatter in the partition coefficients with Al_2O_3 content (**figure 10**) and partly from uncertainty in the calibration of the H_2O measurements using the standards (**figure 2**). A number of crystal profiles are shown, color-coded by crystal, with cores and rims marked. It can be seen that in general the cores grew in more H_2O-rich melts than the rims. This general pattern makes it likely that the zonation is intrinsic to the pyroxene and not related to the interception of small water-bearing inclusions in the crystal. It is also apparent that some crystals exhibit a very large range in H_2O contents from core to rim (these crystals tend to be Al-rich), whilst others show a much narrower range, with oscillatory zoning in both Al_2O_3 and H_2O occurring throughout most of the crystal interior in tandem with only very small or no change in melt H_2O content. This illustrates the strong control of Al in “anchoring” hydrogen in the crystal structure.

401 When melt H_2O contents (calculated from enstatite measurement and calibration) are plotted
402 versus pyroxene Mg#, color-coded for Al_2O_3, it can be observed that in general the lowest Mg#
403 are associated with the highest Al_2O_3 contents and lowest H_2O contents, although there is a
404 broad spread of data (**figure 12**). These trends might be consistent with enstatites being
405 sourced from a range of depths under vapor-saturated conditions, where the "deeper"
406 enstatites are also the most primitive or may reflect the tapping of discrete, heterogeneous
407 magma bodies.
408
409 Melt inclusions hosted by plagioclase in the Soufriere Hills Volcano andesite have been
410 analysed for their H_2O (and CO_2) contents (Edmonds et al., 2014; Humphreys et al., 2010) and
411 these are shown in **figure 12a** for comparison with the pyroxene-derived estimates. Melt
412 inclusions are scarce in the enstatites; only three melt inclusions were analysed (also plotted
413 onto **figure 12b**). The water concentrations measured in the plagioclase-hosted melt
414 inclusions are in general lower than those inferred from the pyroxene compositions. In the melt
415 inclusions measured in enstatite with Mg# 65-67, the water concentrations are around 6 wt%
416 H_2O and are approximately in equilibrium with their host enstatites (**figure 9**). Melt inclusions
417 hosted by plagioclase display a much larger range in their H_2O content. The range in melt H_2O
418 contents might be due to differing degrees of degassing of melt prior to entrapment, different
419 CO_2 concentrations or variable diffusive loss of H^+ (Humphreys et al., 2010). In general, where
420 melt inclusions were measured in enstatites, their water contents overlap with those inferred
421 from their host enstatite H_2O contents, corroborating the melt H_2O contents calculated from the
422 enstatite H_2O and Al_2O_3 systematics. Melt inclusions appear to represent only the more
423 evolved, water-poor end member melts; whereas enstatites, particularly the cores, record
424 higher melt water contents.
425
426 For South Soufriere Hills basalt pyroxenes (**figure 8**), the pyroxene-melt partition coefficient
427 derived from the regression analysis was used to infer the water contents of the melts from
428 which the larger set of pyroxenes (**Table 3**) grew and these are shown in column four of **table**
429 **3**. The inferred melt water concentrations range from 0 to 9.4 wt% and are broadly consistent
430 with the range inferred for the enstatites from the neighbouring Soufriere Hills Volcano
431 andesites.
432
433 *5.4. Reconstruction of vapor saturation pressures*

434 The melt H_2O concentrations derived from the pyroxene compositions (from both Soufriere
435 Hills and South Soufriere Hills volcanoes) may be used to estimate equilibration pressures, but
436 in order to do so the presence of dissolved CO_2 in the melt must be taken into account. The

plagioclase melt inclusions contain up to a few hundred ppm of CO_2 (Edmonds et al., 2014) and large fluxes of gaseous CO_2 have been measured at Soufrière Hills Volcano (Edmonds et al., 2010). Recent work has suggested that arc magmas are fluxed with large quantities of CO_2 (Blundy et al., 2010). The thermodynamic model DCompress (Burgisser et al., 2015) was used to simulate the degassing of melts containing 8 wt% H_2O and both 0.2 and 1 wt% CO_2 and the resulting relationship between crustal depth (assuming a mean crustal density of 2500 kgm^{-3}) and melt water content was parameterised for both cases. The melt inclusion H_2O and CO_2 data for plagioclase-hosted melt inclusions from Soufriere Hills Volcano and the degassing models used are shown in **figure 13**. The resulting depth distributions are shown in **figure 14** as kernel density estimates; saturation pressures estimated for the plagioclase-hosted melt inclusions are also shown. Using a bulk CO_2 content of 0.2 wt% places the mean depth for enstatite equilibration at ~ 10 km. Increasing the CO_2 in the system broadens and deepens the depth distribution. The melt inclusions equilibrated more shallowly (perhaps because they were only sealed off at shallow depths; (Blundy and Cashman, 2005), exhibiting a very broad distribution extending to approximately the same depths as the enstatite data suggests, but also up to the surface. Melt inclusions are far more vulnerable to hydrogen loss by diffusion owing to their much smaller size; this might explain the broader distribution of depths (particularly to shallower depths) for the melt inclusions. The depth ranges compare well with those inferred from clinopyroxene-melt equilibria in South Soufriere Hills basalts (**figure 14C**) (Cassidy et al., 2015b).

5.5. *Diffusive loss of hydrogen from the Soufriere Hills Volcano enstatites*

Diffusive loss or homogenization of hydrogen through the pyroxene structure might erase original magmatic records of water and this process must be considered carefully. There are clearly two end member possibilities: (1) the H^+ in the pyroxene structure is completely decoupled (owing to grossly different diffusive timescales) from the silicate framework of the mineral and responds rapidly to external crustal conditions, whereas the silicate structural framework is essentially frozen, preserving a structure acquired in the lower crust. In this case, the recorded H^+ throughout the crystals would be some product of hydrogen fugacity in the shallow magma, or its immediate post-emplacement conditions (Skogby, 2006). (2) the alternative is that H^+ is coupled to the silicate structure and the crystal preserves some record of changing melt and partition coefficient conditions, as has been suggested for water in assemblages of mantle megacrysts (Bell et al., 2004). In this case the crystal serves as a record for the water content of the system. An understanding of the diffusivity of hydrogen in Al-bearing enstatites is required to discriminate these possibilities.

Xenolith studies have commonly found that water in olivine is lost diffusively during emplacement (Demouchy and Mackwell, 2003; Denis et al., 2013; Li et al., 2008; Peslier and

474 Luhr, 2006), but water in pyroxenes is not (Peslier and Luhr, 2006; Sundvall and Stalder, 2011;
475 Warren and Hauri, 2014; Xia et al., 2010; Yu et al., 2011). Previous studies on magmatic
476 pyroxenes have concluded that there is little diffusive loss of hydrogen during magma ascent
477 from depth (Nazzareni et al., 2011; Sundvall and Stalder, 2011; Wade et al., 2008). Diffusion
478 experiments for hydrogen, which have found D ≈ 10^{-9}–10^{-12} m^2/s at 1000°C for both olivine and
479 clinopyroxene and 10^{-12}–10^{-13} m^2/s for enstatite at 1000°C (**figure 15A)** (Demouchy and
480 Mackwell, 2003; Farver, 2010; Hercule and Ingrin, 1999; Ingrin and Blanchard, 2006; Ingrin et
481 al., 1995; Kohlstedt and Mackwell, 1998; Mackwell and Kohlstedt, 1990; Stalder and Skogby,
482 2003; Woods et al., 2000). The experiments have all been carried out on near-pure enstatite
483 compositions, at room pressure and often at highly reducing conditions (Hercule and Ingrin,
484 1999; Ingrin and Blanchard, 2006; Ingrin et al., 1995; Stalder and Skogby, 2003; Woods et al.,
485 2000). It is not known how the diffusivity of hydrogen in pyroxene would vary under more
486 realistic conditions pertaining to the crust.

487 It is clear that cations in pyroxene have large effects on partitioning and on diffusivity. It has
488 been shown the hydrogen-occupying defects in pyroxene are controlled by redox reactions
489 involving Fe (Hercule and Ingrin, 1999; Stalder et al., 2007). In synthetic Fe-bearing diopsides,
490 diffusion rates of hydrogen are much slower than for Fe-free diopsides, indicating that diffusion
491 is rate-limited by Fe-diffusion (Sundvall et al., 2009). In a recent review of xenoliths from a
492 range of tectonic settings, Warren and Hauri (2014) show that they have homogeneous
493 pyroxenes and variably dehydrated olivines, suggesting that there is a real and significant
494 difference in the diffusivity of hydrogen between olivines and pyroxenes (both clinopyroxene
495 and orthopyroxene), with the latter being significantly slower. They suggest that the difference
496 might be due to some mechanism of cation-limited diffusion controlled by Fe, Cr or Al.
497
498 Based on available experimental data, for temperatures of 850 °C (the temperature of the
499 Soufrière Hills andesite prior to eruption; (Humphreys et al., 2009b), the log of the diffusivity of
500 hydrogen in enstatite may range from -12.5 to -13.5 (**figure 15A**), although it is conceivable
501 that for natural enstatites containing trivalent cations the diffusivity might be smaller. For the
502 enstatites analysed in this study, hydrogen loss is observed in some crystals at distances of
503 <100 μm away from the rim of the crystal; this is consistent with hydrogen loss during magma
504 ascent towards the surface. Using a simple 1D approximation of a Fickian error function to
505 describe the evolution of a diffusion profile with time (the first two terms of the Taylor series
506 expansion):
507

508 $$L \propto 2\sqrt{\int_0^t D(t')\,dt'}\,, \qquad (1)$$

509
510 the diffusion of hydrogen over diffusion lengthscales of 50-100 microns would take 5 to 13
511 hours (**figure 15B**), requiring high magma ascent rates of >0.2 m/s from 10 km depth (or > 0.1
512 from 5 km), or decompression rates (assuming the magma is at lithostatic pressures) of >
513 0.005 MPa/s. The amphiboles in these samples show no breakdown rims, consistent with
514 ascent rates of >0.02 m/s but there are no other independent constraints on ascent rates
515 (Rutherford and Devine, 2003). We note that the ascent rates estimated here would
516 correspond to maximum strain rates (using a conduit radius of 10–100 m) of about 10^{-1} to 10^{-2}
517 s^{-1} (Gonnermann and Manga, 2003), which would require a magma viscosity of 10^{9}-10^{10} Pas
518 for a glassy response and brittle failure (Papale, 1999). This viscosity would likely be reached
519 in the upper parts of the conduit system (owing to water loss and crystallization), leading to
520 fragmentation. Rapid magma ascent from depth has been recently proposed for the aphyric
521 rhyolitic magma erupted during the Chaiten eruption in 2008, requiring ascent from 4 km over
522 4 hours, equivalent to decompression rates of 0.007 MPa/s or 0.3 m/s (Castro and Dingwell,
523 2009).
524
525
526 **6. Conclusion: a vertically protracted crystal mush with geochemically isolated melts**
527 **and abundant exsolved fluids underlying the volcanoes of southern Montserrat**

528 We propose that the zoning preserved in the large, relatively low temperature enstatites
529 erupted during Vulcanian explosions at Soufrière Hills Volcano preserve a record of prolonged,
530 deep magma storage at depths of 4-16 km, but mainly at a depth of 8-12 km (**figure 14**).
531 Nodules of noritic anorthosite have been observed in the andesite (Humphreys et al., 2009b;
532 Kiddle et al., 2010) and we propose that the enstatites here are fragments of the mush brought
533 to the surface, although this may be constrained by future trace element analysis. We
534 envisage mush reorganisation prompted by mafic magma recharge as a trigger for eruption, in
535 the manner described by (Burgisser and Bergantz, 2011), who invoke a rapid "unzipping" of
536 the crystal mush. Although wholescale mafic intrusion and mush remobilization typically takes
537 place over timescales of months for these highly locked and rigid systems, individual
538 instabilities and overturn events could be produced on much shorter timescales. These
539 mechanisms are consistent with recent proposals that the crustal system develops a complex
540 vertically layered system of mushes, liquids and exsolved fluid layers through the crust over
541 long (inter-eruption; 10^{2}-10^{4}) timescales (Christopher et al., 2015) (**figure 14**). Periods of
542 unrest in this case are proposed to have been caused by instabilities propagating downward
543 through the system, driven by segregation and outgassing of fluids at the top.
544

The hydrogen content of the enstatites and of the melt inclusions suggest that rhyolitic melts are vapor saturated at depths of 10 km and perhaps as deep as 16 km in the crust, which implies that an exsolved gas phase is ubiquitous. The presence of high concentrations of exsolved fluids may promote the remobilization of crystal mushes by percolation and advection (Bachmann and Bergantz, 2006), promoting partial melting of the mush (Huber et al., 2011). Deformation experiments have shown that the presence of a small amount of bubbles in the crystal mush (up to 10 vol%) decreases significantly (by four orders of magnitude) the bulk mush viscosity (Pistone et al., 2013), thereby shortening timescales of deformation and overturn, perhaps promoting the occurrence of large explosive eruptions. Conversely, removal of the exsolved fluid phase from the mush can lead to freezing and "viscous death".

The distinct geochemical signatures of the Soufriere Hills and South Soufriere Hills volcanic products with regard to their trace element and Pb isotope signature (Cassidy et al., 2012) requires them to have been stored in physically distinct reservoirs prior to eruption, yet the results of this study suggest that both volcanoes tap magma from the same depth range at a lateral distance of only 1-2 km. These features might be consistent with the existence of isolated, smaller scale melt bodies within the crystal mush, lending support to the emerging picture of a heterogeneous, vertically and laterally extensive crystal mush system, similar to that proposed recently for the magmatic system beneath the island of Dominica (Howe et al., 2015) and the Taupo Volcanic Zone, New Zealand (Bégué et al., 2015).

The enstatite crystals preserve narrow zones at the crystal margins where hydrogen was lost by diffusion after degassing of the carrier liquid, which constrains magma ascent times from depth to the surface to be up 5-13 hours. These findings confirm that Vulcanian explosions at Montserrat are driven by deep-seated changes in reservoir overpressure and that cyclicity with ~ 12 hour periods at the surface may reflect timescales of ascent of magma batches from depth. Magma ascent on these rapid timescales lie largely within the viscous regime, with fragmentation expected to occur in the top 1 km of the system as degassing and crystallisation increase bulk magma viscosity. The presence of large amounts of exsolved vapour in the magmatic system at these depths raises the possibility that overpressures for rapid magma ascent (and explosive eruption) might be caused by fluid generation and instabilities within the mush.

Acknowledgements

ME acknowledges NERC grant NE/I016694/1 and NERC ion probe facility grant IMF429/0511 and Cees-Jan de Hoog, who provided invaluable assistance with SIMS measurements and

582 calibration. MC acknowledges an Alexander Von Humboldt fellowship. Adam Kent and Nicole
583 Metrich provided extremely helpful reviews.

584

585

586 **References**

587

588 Annen, C., Blundy, J., Sparks, R., 2006. The genesis of intermediate and silicic magmas in deep crustal hot zones.
589 Journal of Petrology 47, 505-539.
590 Aubaud, C., Hauri, E.H., Hirschmann, M.M., 2004. Hydrogen partition coefficients between nominally anhydrous
591 minerals and basaltic melts. Geophysical Research Letters 31.
592 Bachmann, O., Bergantz, G.W., 2006. Gas percolation in upper-crustal silicic crystal mushes as a mechanism for
593 upward heat advection and rejuvenation of near-solidus magma bodies. Journal of Volcanology and Geothermal
594 Research 149, 85-102.
595 Bacon, C.R., 1986. Magmatic inclusions in silicic and intermediate volcanic rocks. Journal of Geophysical Research:
596 Solid Earth 91, 6091-6112.
597 Baker, M.B., Grove, T.L., Price, R., 1994. Primitive basalts and andesites from the Mt. Shasta region, N. California:
598 products of varying melt fraction and water content. Contr. Mineral. and Petrol. 118, 111-129.
599 Bégué, F., Gravley, D.M., Chambefort, I., Deering, C.D., Kennedy, B.M., 2015. Magmatic volatile distribution as
600 recorded by rhyolitic melt inclusions in the Taupo Volcanic Zone, New Zealand. Geological Society, London, Special
601 Publications 410, 71-94.
602 Bell, D.R., Rossman, G.R., 1992. Water in Earth's mantle: The role of nominally anhydrous minerals. Science 255,
603 1391-1397.
604 Bell, D.R., Rossman, G.R., Moore, R.O., 2004. Abundance and partitioning of OH in a high-pressure magmatic
605 system: megacrysts from the Monastery kimberlite, South Africa. Journal of Petrology 45, 1539-1564.
606 Bergantz, G., Schleicher, J., Burgisser, A., 2015. Open-system dynamics and mixing in magma mushes. Nature
607 Geoscience 8, 793-796.
608 Blundy, J., Cashman, K., 2005. Rapid decompression-driven crystallization recorded by melt inclusions from Mount
609 St. Helens volcano. Geology 33, 793-796.
610 Blundy, J., Cashman, K., 2008. Petrologic Reconstruction of Magmatic System Variables and Processes. Reviews
611 in Mineralogy and Geochemistry 69, 179-239.
612 Blundy, J., Cashman, K.V., Rust, A., Witham, F., 2010. A case for CO 2-rich arc magmas. Earth and Planetary
613 Science Letters 290, 289-301.
614 Burgisser, A., Alletti, M., Scaillet, B., 2015. Simulating the behavior of volatiles belonging to the C–O–H–S system in
615 silicate melts under magmatic conditions with the software D-Compress. Computers & Geosciences 79, 1-14.
616 Burgisser, A., Bergantz, G.W., 2011. A rapid mechanism to remobilize and homogenize highly crystalline magma
617 bodies. Nature 471, 212-215.
618 Cashman, K., Blundy, J., 2000. Degassing and crystallization of ascending andesite and dacite. Philosophical
619 Transactions of the Royal Society of London. Series A: Mathematical, Physical and Engineering Sciences 358,
620 1487-1513.
621 Cashman, K., Blundy, J., 2013. Petrological cannibalism: the chemical and textural consequences of incremental
622 magma body growth. Contr. Mineral. and Petrol. 166, 703-729.
623 Cashman, K.V., Sparks, R.S.J., 2013. How volcanoes work: A 25 year perspective. Geological Society of America
624 Bulletin 125, 664-690.
625 Cassidy, M., Edmonds, M., Watt, S.F., Palmer, M.R., Gernon, T.M., 2015a. Origin of Basalts by Hybridization in
626 Andesite-dominated Arcs. Journal of Petrology, egv002.
627 Cassidy, M., Taylor, R., Palmer, M., Cooper, R., Stenlake, C., Trofimovs, J., 2012. Tracking the magmatic evolution
628 of island arc volcanism: Insights from a high-precision Pb isotope record of Montserrat, Lesser Antilles.
629 Geochemistry, Geophysics, Geosystems 13.
630 Cassidy, M., Watt, S., Talling, P., Palmer, M., Edmonds, M., Jutzeler, M., Wall-Palmer, D., Manga, M., Coussens,
631 M., Gernon, T., 2015b. Rapid onset of mafic magmatism facilitated by volcanic edifice collapse. Geophysical
632 Research Letters.
633 Castro, J.M., Dingwell, D.B., 2009. Rapid ascent of rhyolitic magma at Chaitén volcano, Chile. Nature 461, 780-783.
634 Cervantes, P., Wallace, P.J., 2003. Role of H2O in subduction-zone magmatism: new insights from melt inclusions
635 in high-Mg basalts from central Mexico. Geology 31, 235-238.
636 Christopher, T., Blundy, J., Cashman, K., Cole, P., Edmonds, M., Smith, P., Sparks, R., Stinton, A., 2015. Crustal-
637 scale degassing due to magma system destabilization and magma-gas decoupling at Soufrière Hills Volcano,
638 Montserrat. Geochemistry, Geophysics, Geosystems.
639 Clarke, A., Stephens, S., Teasdale, R., Sparks, R., Diller, K., 2007. Petrologic constraints on the decompression
640 history of magma prior to Vulcanian explosions at the Soufrière Hills volcano, Montserrat. Journal of Volcanology
641 and Geothermal Research 161, 261-274.
642 Cooper, K.M., Kent, A.J., 2014. Rapid remobilization of magmatic crystals kept in cold storage. Nature.
643 Couch, S., Sparks, R., Carroll, M., 2001. Mineral disequilibrium in lavas explained by convective self-mixing in open
644 magma chambers. Nature 411, 1037-1039.

Demouchy, S., Mackwell, S., 2003. Water diffusion in synthetic iron-free forsterite. Physics and Chemistry of Minerals 30, 486-494.
Denis, C.M., Demouchy, S., Shaw, C.S., 2013. Evidence of dehydration in peridotites from Eifel Volcanic Field and estimates of the rate of magma ascent. Journal of Volcanology and Geothermal Research 258, 85-99.
Devine, J., Rutherford, M., Norton, G., Young, S., 2003. Magma storage region processes inferred from geochemistry of Fe–Ti oxides in andesitic magma, Soufriere Hills Volcano, Montserrat, WI. Journal of Petrology 44, 1375-1400.
Devine, J.D., Gardner, J.E., Brack, H.P., Layne, G.D., Rutherford, M.J., 1995. Comparison of microanalytical methods for estimating H2O contents of silicic volcanic glasses. American Mineralogist 80, 319-328.
Dixon, J.E., Clague, D.A., Stolper, E.M., 1991. Degassing history of water, sulfur, and carbon in submarine lavas from Kīlauea Volcano, Hawaii. The Journal of Geology, 371-394.
Dobson, P.F., Skogby, H., Rossman, G.R., 1995. Water in boninite glass and coexisting orthopyroxene: concentration and partitioning. Contr. Mineral. and Petrol. 118, 414-419.
Druitt, T., Young, S., Baptie, B., Bonadonna, C., Calder, E., Clarke, A., Cole, P., Harford, C., Herd, R., Luckett, R., 2002. Episodes of cyclic Vulcanian explosive activity with fountain collapse at Soufrière Hills Volcano, Montserrat. MEMOIRS-GEOLOGICAL SOCIETY OF LONDON 21, 281-306.
Edmonds, M., Aiuppa, A., Humphreys, M., Moretti, R., Giudice, G., Martin, R., Herd, R., Christopher, T., 2010. Excess volatiles supplied by mingling of mafic magma at an andesite arc volcano. Geochemistry, Geophysics, Geosystems 11.
Edmonds, M., Herd, R.A., Strutt, M.H., 2006. Tephra deposits associated with a large lava dome collapse, Soufrière Hills Volcano, Montserrat, 12–15 July 2003. Journal of volcanology and geothermal research 153, 313-330.
Edmonds, M., Humphreys, M.C., Hauri, E.H., Herd, R.A., Wadge, G., Rawson, H., Ledden, R., Plail, M., Barclay, J., Aiuppa, A., 2014. Pre-eruptive vapour and its role in controlling eruption style and longevity at Soufrière Hills Volcano. Geological Society, London, Memoirs 39, 291-315.
Elsworth, D., Mattioli, G., Taron, J., Voight, B., Herd, R., 2008. Implications of magma transfer between multiple reservoirs on eruption cycling. Science 322, 246-248.
Esposito, R., Hunter, J., Schiffbauer, J.D., Bodnar, R.J., 2014. An assessment of the reliability of melt inclusions as recorders of the pre-eruptive volatile content of magmas. American Mineralogist 99, 976-998.
Evans, K., Elburg, M., Kamenetsky, V., 2012. Oxidation state of subarc mantle. Geology 40, 783-786.
Farver, J.R., 2010. Oxygen and hydrogen diffusion in minerals. Reviews in Mineralogy and Geochemistry 72, 447-507.
Faure, F., Schiano, P., 2005. Experimental investigation of equilibration conditions during forsterite growth and melt inclusion formation. Earth and Planetary Science Letters 236, 882-898.
Gaetani, G.A., Grove, T.L., Bryan, W.B., 1993. The influence of water on the petrogenesis of subductionrelated igneous rocks. Nature 365, 332-334.
Gaetani, G.A., O'Leary, J.A., Shimizu, N., Bucholz, C.E., Newville, M., 2012. Rapid reequilibration of H2O and oxygen fugacity in olivine-hosted melt inclusions. Geology 40, 915-918.
Giachetti, T., Druitt, T., Burgisser, A., Arbaret, L., Galven, C., 2010. Bubble nucleation, growth and coalescence during the 1997 Vulcanian explosions of Soufrière Hills Volcano, Montserrat. Journal of Volcanology and Geothermal Research 193, 215-231.
Gonnermann, H.M., Manga, M., 2003. Explosive volcanism may not be an inevitable consequence of magma fragmentation. Nature 426, 432-435.
Grant, K., Ingrin, J., Lorand, J.P., Dumas, P., 2007a. Water partitioning between mantle minerals from peridotite xenoliths. Contr. Mineral. and Petrol. 154, 15-34.
Grant, K.J., Kohn, S.C., Brooker, R.A., 2006. Solubility and partitioning of water in synthetic forsterite and enstatite in the system MgO–SiO2–H2O±Al2O3. Contr. Mineral. and Petrol. 151, 651-664.
Grant, K.J., Kohn, S.C., Brooker, R.A., 2007b. The partitioning of water between olivine, orthopyroxene and melt synthesised in the system albite–forsterite–H< sub> 2</sub> O. Earth and Planetary Science Letters 260, 227-241.
Grove, T.L., Kinzler, R.J., 1986. Petrogenesis of andesites. Annual Review of Earth and Planetary Sciences 14, 417.
Harford, C., Pringle, M., Sparks, R., Young, S., 2002. The volcanic evolution of Montserrat using 40Ar/39Ar geochronology. Geological Society, London, Memoirs 21, 93-113.
Hartley, M.E., Maclennan, J., Edmonds, M., Thordarson, T., 2014. Reconstructing the deep CO< sub> 2</sub> degassing behaviour of large basaltic fissure eruptions. Earth and Planetary Science Letters 393, 120-131.
Hauri, E., 2002. SIMS analysis of volatiles in silicate glasses, 2: isotopes and abundances in Hawaiian melt inclusions. Chemical Geology 183, 115-141.
Hauri, E.H., Gaetani, G.A., Green, T.H., 2006. Partitioning of water during melting of the Earth's upper mantle at H< sub> 2</sub> O-undersaturated conditions. Earth and Planetary Science Letters 248, 715-734.
Hautmann, S., Gottsmann, J., Sparks, R.S.J., Mattioli, G.S., Sacks, I.S., Strutt, M.H., 2010. Effect of mechanical heterogeneity in arc crust on volcano deformation with application to Soufrière Hills Volcano, Montserrat, West Indies. Journal of Geophysical Research: Solid Earth (1978–2012) 115.
Hercule, S., Ingrin, J., 1999. Hydrogen in diopside: Diffusion, kinetics of extraction-incorporation, and solubility. American Mineralogist 84, 1577-1587.
Howe, T., Lindsay, J., Shane, P., 2015. Evolution of young andesitic–dacitic magmatic systems beneath Dominica, Lesser Antilles. Journal of Volcanology and Geothermal Research 297, 69-88.

710 Huber, C., Bachmann, O., Dufek, J., 2011. Thermo-mechanical reactivation of locked crystal mushes: Melting-
711 induced internal fracturing and assimilation processes in magmas. Earth and Planetary Science Letters 304, 443-
712 454.
713 Humphreys, M., Edmonds, M., Christopher, T., Hards, V., 2009a. Chlorine variations in the magma of Soufrière Hills
714 Volcano, Montserrat: Insights from Cl in hornblende and melt inclusions. Geochimica et Cosmochimica Acta 73,
715 5693-5708.
716 Humphreys, M., Edmonds, M., Christopher, T., Hards, V., 2010. Magma hybridisation and diffusive exchange
717 recorded in heterogeneous glasses from Soufrière Hills Volcano, Montserrat. Geophysical Research Letters 37.
718 Humphreys, M.C., Blundy, J.D., Sparks, R.S.J., 2006. Magma evolution and open-system processes at Shiveluch
719 Volcano: insights from phenocryst zoning. Journal of Petrology 47, 2303-2334.
720 Humphreys, M.C., Christopher, T., Hards, V., 2009b. Microlite transfer by disaggregation of mafic inclusions
721 following magma mixing at Soufrière Hills volcano, Montserrat. Contr. Mineral. and Petrol. 157, 609-624.
722 Ingrin, J., Blanchard, M., 2006. Diffusion of hydrogen in minerals. Reviews in mineralogy and geochemistry 62, 291-
723 320.
724 Ingrin, J., Hercule, S., Charton, T., 1995. Diffusion of hydrogen in diopside: results of dehydration experiments.
725 Journal of Geophysical Research: Solid Earth (1978–2012) 100, 15489-15499.
726 Kent, A.J., Elliott, T.R., 2002. Melt inclusions from Marianas arc lavas: implications for the composition and
727 formation of island arc magmas. Chemical Geology 183, 263-286.
728 Kiddle, E., Edwards, B., Loughlin, S., Petterson, M., Sparks, R., Voight, B., 2010. Crustal structure beneath
729 Montserrat, Lesser Antilles, constrained by xenoliths, seismic velocity structure and petrology. Geophysical
730 Research Letters 37.
731 Koga, K., Hauri, E., Hirschmann, M., Bell, D., 2003. Hydrogen concentration analyses using SIMS and FTIR:
732 comparison and calibration for nominally anhydrous minerals. Geochemistry, Geophysics, Geosystems 4.
733 Kohlstedt, D.L., Mackwell, S.J., 1998. Diffusion of hydrogen and intrinsic point defects in olivine. Zeitschrift für
734 physikalische Chemie 207, 147-162.
735 Kohn, S.C., Grant, K.J., 2006. The partitioning of water between nominally anhydrous minerals and silicate melts.
736 Reviews in mineralogy and geochemistry 62, 231-241.
737 Lange, R.A., Frey, H.M., Hector, J., 2009. A thermodynamic model for the plagioclase-liquid
738 hygrometer/thermometer. American Mineralogist 94, 494-506.
739 Li, Z.X.A., Lee, C.T.A., Peslier, A.H., Lenardic, A., Mackwell, S.J., 2008. Water contents in mantle xenoliths from the
740 Colorado Plateau and vicinity: Implications for the mantle rheology and hydration‐induced thinning of continental
741 lithosphere. Journal of Geophysical Research: Solid Earth (1978–2012) 113.
742 Lloyd, A., Plank, T., Ruprecht, P., Hauri, E., Rose, W., 2013. Timescales of magma ascent recorded by H2O
743 zonation in clinopyroxene, AGU Fall Meeting Abstracts, p. 2718.
744 Lowenstern, J.B., 1995. Applications of silicate-melt inclusions to the study of magmatic volatiles. Magmas, fluids,
745 and ore deposits 23, 71-99.
746 Mackwell, S.J., Kohlstedt, D.L., 1990. Diffusion of hydrogen in olivine: implications for water in the mantle. Journal
747 of Geophysical Research: Solid Earth (1978–2012) 95, 5079-5088.
748 Melnik, O., Costa, A., 2014. Dual-chamber-conduit models of non-linear dynamics behaviour at Soufrière Hills
749 Volcano, Montserrat. Geological Society, London, Memoirs 39, 61-69.
750 Melnik, O., Sparks, R., 2002. Dynamics of magma ascent and lava extrusion at Soufrière Hills Volcano, Montserrat.
751 Geological Society, London, Memoirs 21, 153-171.
752 Métrich, N., Wallace, P.J., 2008. Volatile Abundances in Basaltic Magmas and Their Degassing Paths Tracked by
753 Melt Inclusions. Reviews in Mineralogy and Geochemistry 69, 363-402.
754 Mierdel, K., Keppler, H., 2004. The temperature dependence of water solubility in enstatite. Contr. Mineral. and
755 Petrol. 148, 305-311.
756 Moore, L.R., Gazel, E., Tuohy, R., Lloyd, A.S., Esposito, R., Steele-MacInnis, M., Hauri, E.H., Wallace, P.J., Plank,
757 T., Bodnar, R.J., 2015. Special Collection: Glasses, Melts, and Fluids, as Tools for Understanding Volcanic
758 Processes and Hazards. Bubbles matter: An assessment of the contribution of vapor bubbles to melt inclusion
759 volatile budgets. American Mineralogist 100, 806-823.
760 Murphy, M., Sparks, R., Barclay, J., Carroll, M., Brewer, T., 2000. Remobilization of andesite magma by intrusion of
761 mafic magma at the Soufriere Hills Volcano, Montserrat, West Indies. Journal of petrology 41, 21-42.
762 Nakamura, M., Shimakita, S., 1998. Dissolution origin and syn-entrapment compositional change of melt inclusion
763 in plagioclase. Earth and Planetary Science Letters 161, 119-133.
764 Nazzareni, S., Skogby, H., Zanazzi, P., 2011. Hydrogen content in clinopyroxene phenocrysts from Salina mafic
765 lavas (Aeolian arc, Italy). Contr. Mineral. and Petrol. 162, 275-288.
766 Neave, D.A., Passmore, E., Maclennan, J., Fitton, G., Thordarson, T., 2013. Crystal–melt relationships and the
767 record of deep mixing and crystallization in the ad 1783 Laki Eruption, Iceland. Journal of Petrology, egt027.
768 O'Leary, J.A., Gaetani, G.A., Hauri, E.H., 2010. The effect of tetrahedral Al< sup> 3+</sup> on the partitioning of
769 water between clinopyroxene and silicate melt. Earth and Planetary Science Letters 297, 111-120.
770 Papale, P., 1999. Strain-induced magma fragmentation in explosive eruptions. Nature 397, 425-428.
771 Paulatto, M., Minshull, T., Baptie, B., Dean, S., Hammond, J., Henstock, T., Kenedi, C., Kiddle, E., Malin, P., Peirce,
772 C., 2010. Upper crustal structure of an active volcano from refraction/reflection tomography, Montserrat, Lesser
773 Antilles. Geophysical Journal International 180, 685-696.
774 Peslier, A.H., Luhr, J.F., 2006. Hydrogen loss from olivines in mantle xenoliths from Simcoe (USA) and Mexico:
775 mafic alkalic magma ascent rates and water budget of the sub-continental lithosphere. Earth and Planetary Science
776 Letters 242, 302-319.

Petford, N., Gallagher, K., 2001. Partial melting of mafic (amphibolitic) lower crust by periodic influx of basaltic magma. Earth and Planetary Science Letters 193, 483-499.
Pistone, M., Arzilli, F., Dobson, K.J., Cordonnier, B., Reusser, E., Ulmer, P., Marone, F., Whittington, A.G., Mancini, L., Fife, J.L., 2015. Gas-driven filter pressing in magmas: Insights into in-situ melt segregation from crystal mushes. Geology 43, 699-702.
Pistone, M., Caricchi, L., Ulmer, P., Reusser, E., Ardia, P., 2013. Rheology of volatile-bearing crystal mushes: mobilization vs. viscous death. Chemical Geology 345, 16-39.
Plail, M., Barclay, J., Humphreys, M.C., Edmonds, M., Herd, R.A., Christopher, T.E., 2014. Characterization of mafic enclaves in the erupted products of Soufrière Hills Volcano, Montserrat, 2009 to 2010. Geological Society, London, Memoirs 39, 343-360.
Plank, T., Kelley, K.A., Zimmer, M.M., Hauri, E.H., Wallace, P.J., 2013. Why do mafic arc magmas contain∼ 4wt% water on average? Earth and Planetary Science Letters 364, 168-179.
Putirka, K., Johnson, M., Kinzler, R., Longhi, J., Walker, D., 1996. Thermobarometry of mafic igneous rocks based on clinopyroxene-liquid equilibria, 0–30 kbar. Contr. Mineral. and Petrol. 123, 92-108.
Rauch, M., Keppler, H., 2002. Water solubility in orthopyroxene. Contr. Mineral. and Petrol. 143, 525-536.
Ridolfi, F., Renzulli, A., Puerini, M., 2010. Stability and chemical equilibrium of amphibole in calc-alkaline magmas: an overview, new thermobarometric formulations and application to subduction-related volcanoes. Contr. Mineral. and Petrol. 160, 45-66.
Roggensack, K., Hervig, R.L., McKnight, S.B., Williams, S.N., 1997. Explosive basaltic volcanism from Cerro Negro volcano: influence of volatiles on eruptive style. Science 277, 1639-1642.
Rosenthal, A., Hauri, E., Hirschmann, M., 2015. Experimental determination of C, F, and H partitioning between mantle minerals and carbonated basalt, CO 2/Ba and CO 2/Nb systematics of partial melting, and the CO 2 contents of basaltic source regions. Earth and Planetary Science Letters 412, 77-87.
Rüpke, L.H., Morgan, J.P., Hort, M., Connolly, J.A., 2004. Serpentine and the subduction zone water cycle. Earth and Planetary Science Letters 223, 17-34.
Ruprecht, P., Bergantz, G.W., Cooper, K.M., Hildreth, W., 2012. The crustal magma storage system of Volcán Quizapu, Chile, and the effects of magma mixing on magma diversity. Journal of Petrology, egs002.
Rutherford, M.J., Devine, J.D., 2003. Magmatic conditions and magma ascent as indicated by hornblende phase equilibria and reactions in the 1995–2002 Soufriere Hills magma. Journal of Petrology 44, 1433-1453.
Scaillet, B., Clémente, B., Evans, B.W., Pichavant, M., 1998. Redox control of sulfur degassing in silicic magmas. Journal of Geophysical Research: Solid Earth (1978–2012) 103, 23937-23949.
Sevilla, W.I., Ammon, C.J., Voight, B., De Angelis, S., 2010. Crustal structure beneath the Montserrat region of the Lesser Antilles island arc. Geochemistry, Geophysics, Geosystems 11.
Shalev, E., Kenedi, C., Malin, P., Voight, V., Miller, V., Hidayat, D., Sparks, R., Minshull, T., Paulatto, M., Brown, L., 2010. Three‐dimensional seismic velocity tomography of Montserrat from the SEA‐CALIPSO offshore/onshore experiment. Geophysical Research Letters 37.
Sides, I., Edmonds, M., Maclennan, J., Houghton, B., Swanson, D., Steele-MacInnis, M., 2014. Magma mixing and high fountaining during the 1959 Kīlauea Iki eruption, Hawai ʻi. Earth and Planetary Science Letters 400, 102-112.
Sisson, T., Bacon, C., 1999. Gas-driven filter pressing in magmas. Geology 27, 613-616.
Skogby, H., 2006. Water in natural mantle minerals I: pyroxenes. Reviews in mineralogy and geochemistry 62, 155-167.
Spera, F.J., 1984. Carbon dioxide in petrogenesis III: role of volatiles in the ascent of alkaline magma with special reference to xenolith-bearing mafic lavas. Contr. Mineral. and Petrol. 88, 217-232.
Stalder, R., Purwin, H., Skogby, H., 2007. Influence of Fe on hydrogen diffusivity in orthopyroxene. European Journal of Mineralogy 19, 899-903.
Stalder, R., Skogby, H., 2002. Hydrogen incorporation in enstatite. European Journal of Mineralogy 14, 1139-1144.
Stalder, R., Skogby, H., 2003. Hydrogen diffusion in natural and synthetic orthopyroxene. Physics and Chemistry of Minerals 30, 12-19.
Stamper, C., Melekhova, E., Blundy, J., Arculus, R., Humphreys, M., Brooker, R., 2014. Oxidised phase relations of a primitive basalt from Grenada, Lesser Antilles. Contr. Mineral. and Petrol. 167, 1-20.
Steele-Macinnis, M., Esposito, R., Bodnar, R.J., 2011. Thermodynamic model for the effect of post-entrapment crystallization on the H2O–CO2 systematics of vapor-saturated, silicate melt inclusions. Journal of Petrology 52, 2461-2482.
Sundvall, R., Skogby, H., Stalder, R., 2009. Dehydration-hydration mechanisms in synthetic Fe-poor diopside. European journal of mineralogy 21, 17-26.
Sundvall, R., Stalder, R., 2011. Water in upper mantle pyroxene megacrysts and xenocrysts: A survey study. American Mineralogist 96, 1215-1227.
Tenner, T.J., Hirschmann, M.M., Withers, A.C., Hervig, R.L., 2009. Hydrogen partitioning between nominally anhydrous upper mantle minerals and melt between 3 and 5 GPa and applications to hydrous peridotite partial melting. Chemical Geology 262, 42-56.
Wade, J.A., Plank, T., Hauri, E.H., Kelley, K.A., Roggensack, K., Zimmer, M., 2008. Prediction of magmatic water contents via measurement of H2O in clinopyroxene phenocrysts. Geology 36, 799-802.
Wadge, G., Voight, B., Sparks, R., Cole, P., Loughlin, S., Robertson, R., 2014. An overview of the eruption of Soufriere Hills Volcano, Montserrat from 2000 to 2010. Geological Society, London, Memoirs 39, 1-40.
Walker, J.A., Roggensack, K., Patino, L.C., Cameron, B.I., Matías, O., 2003. The water and trace element contents of melt inclusions across an active subduction zone. Contr. Mineral. and Petrol. 146, 62-77.

Wallace, P.J., Edmonds, M., 2011. The sulfur budget in magmas: evidence from melt inclusions, submarine glasses, and volcanic gas emissions. Reviews in Mineralogy and Geochemistry 73, 215-246.
Wallace, P.J., Kamenetsky, V.S., Cervantes, P., 2015. Melt inclusion CO2 contents, pressures of olivine crystallization, and the problem of shrinkage bubbles. American Mineralogist 100, 787-794.
Warren, J.M., Hauri, E.H., 2014. Pyroxenes as tracers of mantle water variations. Journal of Geophysical Research: Solid Earth 119, 1851-1881.
Weis, F.A., Skogby, H., Troll, V.R., Deegan, F.M., Dahren, B., 2015. Magmatic water contents determined through clinopyroxene: Examples from the Western Canary Islands, Spain. Geochemistry, Geophysics, Geosystems.
Williams-Jones, A.E., Heinrich, C.A., 2005. 100th Anniversary special paper: vapor transport of metals and the formation of magmatic-hydrothermal ore deposits. Economic Geology 100, 1287-1312.
Woods, S.C., Mackwell, S., Dyar, D., 2000. Hydrogen in diopside: Diffusion profiles. American Mineralogist 85, 480-487.
Xia, Q.K., Hao, Y., Li, P., Deloule, E., Coltorti, M., Dallai, L., Yang, X., Feng, M., 2010. Low water content of the Cenozoic lithospheric mantle beneath the eastern part of the North China Craton. Journal of Geophysical Research: Solid Earth (1978–2012) 115.
Yu, Y., Xu, X.-S., Griffin, W.L., O'Reilly, S.Y., Xia, Q.-K., 2011. H< sub> 2</sub> O contents and their modification in the Cenozoic subcontinental lithospheric mantle beneath the Cathaysia block, SE China. Lithos 126, 182-197.
Zajacz, Z., Halter, W., 2009. Copper transport by high temperature, sulfur-rich magmatic vapor: Evidence from silicate melt and vapor inclusions in a basaltic andesite from the Villarrica volcano (Chile). Earth and Planetary Science Letters 282, 115-121.

Figure captions

Figure 1: Locational and volcanic context of the present study. A: map of the island of Montserrat, showing the Soufriere Hills Volcano as a triangle in the centre of southern portion of the island. Pumices for this study were collected at Cork Hill and Spring Estate, to the west of the volcano. Inset map shows the location of Montserrat in the Lesser Antilles. B: a typical Vulcanian explosion at Soufriere Hills Volcano, showing the development of an ashy eruption column and collapse-generated pyroclastic flows. C: Isopach map for the Vulcanian explosion on 15 July 2003 which produced the pumices studied here; solid lines: lithic fragment sizes and dashed lines: pumice sizes, in mm (Edmonds et al., 2006).

Figure 2: Petrographic context of the enstatites in the Soufriere Hills Volcano (Montserrat, West Indies) andesite. A: photomicrograph to show the margin of a mafic enclave (bottom) and the andesite host (top). Phases are labelled, including orthopyroxene (opx), plagioclase (plag), magnetite (mgt), hornblende (hbl), glass (gl) and vesicles (ves). B and C: backscattered electron images of orthopyroxenes, showing their euhedral shape, thin Mg-rich overgrowths and melt inclusions (dark rounded inclusions).

Figure 3: Calibration curves for A: the 6f ion microprobe at the Carnegie Institution, showing the measured OH/Si ratio plotted against the water content of well-characterised glass standards; B: the 4f ion microprobe at the NERC facility at the University of Edinburgh, with measured H/Si plotted against the water content of a set of standards and C: pyroxene water content, with the measured OH/Si ratio plotted against the water content of a range of orthopyroxene standards (Hauri et al., 2006).

Figure 4: Major element composition of the Soufriere Hills Volcano enstatities in wt% measured by electron microprobe, showing A: MgO against SiO_2; B: MgO against FeO_{tot}; C: MgO against Al_2O_3; and D: Al_2O_3 against distance from crystal rim (microns). Uncertainties are shown by the ellipse.

Figure 5: Plots to show the co-variation of H_2O (measured by SIMS) and aluminium (measured by electron microprobe) in the enstatites from the Soufriere Hills Volcano andesite. A: Plot of H_2O content of the enstatite in ppm plotted against Al_2O_3 (wt%), color-coded for pyroxene Mg#. B: Plot of molar H/Al ratio against Al_2O_3, color-coded for pyroxene Mg#. C: Plot of molar H/Al ratio against Al_2O_3, color-coded for enstatite H_2O content (ppm).

Figure 6: Typical profiles through indium-mounted enstatites in andesites from Soufriere Hills Volcano (Montserrat). Left: reflected light images to show surface of enstatite with crystallographic directions and the SIMS profiles marked. Right: H_2O and molar H/Al plotted against distance from crystal rim.

Figure 7: Water contents of pyroxenes and melt inclusions from South Soufriere Hills Volcano (Montserrat, West Indies) basalts.

Figure 8: Plot to show Soufriere Hills Volcano enstatite water content plotted against distance from crystal rim, color-cided for Al_2O_3 content. Uncertainty shown by the ellipse.

Figure 9: Schematic diagram to show how zoning in H_2O and in molar H/Al might be interpreted under the conditions of A: constant melt H_2O, with the enstatite zoned in Al_2O_3; B: variable melt H_2O contents (due to degassing or vapor-undersaturated fractionation, for example) with a homogeneous enstatite and C: variable melt H_2O and a zoned enstatite.

Figure 10: Relationship between enstatite Al_2O_3 content and crystal-melt partition coefficient for H_2O, constrained by experiment and analysis by various workers (shown in legend). A: regression through the data color-coded by study. The equation relating D and Al content of enstatite used in this study is shown. B: the data are color-coded for the activitity of water in the coexisting melt.

Figure 11: Plot of Soufriere Hills Volcano enstatite Al_2O_3 content against H_2O content, contoured for melt H_2O content, calculated using the regression shown in **figure 10**. Individual crystal zoning pathways are marked on with a single color, and the core and rim concentrations are labelled.

927

928 **Figure 12**: Left: a kernel density estimate (KDE) of melt inclusion water concentrations
929 (Humphreys et al., 2010) and right: melt water contents (calculated from enstatite water
930 content) plotted against enstatite Mg#, color-coded for enstatite Al_2O_3 content. The water
931 content of the melt inclusions hosted by enstatite are shown by the smaller grey rectangles,
932 plotted at the Mg# of the host enstatite adjacent to the melt inclusion. Uncertainties are
933 indicated by the ellipse.
934

935 **Figure 13**: A: Melt inclusion H_2O and CO_2 concentrations, meaured by SIMS (Edmonds et al.,
936 2014; Humphreys et al., 2009a). Grey symbols are measured using the Carnegie Institution 6f
937 and black the NERC 4f ion probes. Isobars are solid lines and represent 100, 200 and 300
938 MPa from left to right and dotted lines are isopleths, representing melts in equlibrium with a
939 gas phase containing 55, 75 and 90 mol% CO_2 from top to bottom. B: Model of CO_2 and H_2O
940 degassing, using bulk CO_2 contents of 0.2 and 1.0 wt%, using thermodynamic model
941 Dcompress (Burgisser et al., 2015), color-coded for depth in km, assuming lithostatic pressure
942 and a crustal density of 2500 kgm^{-3}.
943

944 **Figure 14**: Schematic diagram showing the possible magmatic architecture beneath Soufriere
945 Hills Volcano, based partly on this work and partly on others (Cassidy et al., 2015a;
946 Christopher et al., 2015; Elsworth et al., 2008; Kiddle et al., 2010). Right: kernel density
947 estimates (KDE) of depth ranges estimated from H_2O-CO_2 barometry on plagioclase melt
948 inclusions and on the H content of enstatite, assuming two bulk CO_2 contents (see text).
949 Depths of equilibration estimated from clinopyroxene-liquid equilibria for the products of South
950 Soufriere Hills Volcano are also shown (Cassidy et al., 2015b).
951

952 **Figure 15**: A: Diffusivity data for hydrogen in diopsides from the literature (red curves) (Hercule
953 and Ingrin, 1999; Ingrin et al., 1995; Woods et al., 2000) compared to diffusion in olivine
954 (black) (Demouchy and Mackwell, 2003) and in enstatite (Stalder and Skogby, 2003). The
955 fraction of Mg with respect to the total molar abundance of Mg and Fe is shown on the right, in
956 black. Crystallographic orientation is shown in square brackets for each curve. B: Timescales
957 estimated from diffusion profiles in hydrogen at enstatite rims, versus diffusion lengthscales,
958 contoured for diffusivity. Grey shaded area shows region constrained by lengthscales and by
959 experimental diffusivities.
960

961 **Tables**
962

963 **Table 1**: Major element and H_2O concentrations in enstatites in andesites from Soufriere Hills
964 Volcano (Montserrat, West Indies), measured by EPMA and by SIMS respectively. Details of
965 analytical procedures, uncertainties and calibration given in the text. Concentrations of the
966 major and minor elements are given in wt%; b.d.: below detection. D: distance from rim of
967 crystal, in microns. Mg# is the molar percentage of atomic Mg as a percentage of the sum of
968 atomic Mg and Fe in the pyroxene. Water concentrations are in ppm.
969
970 **Table 2**: The composition of pyroxenes from South Soufriere Hills Volcano (Montserrat, West
971 Indies), measured by electron microprobe. Element oxide concentrations are shown in wt%
972
973 **Table 3**: The water contents of augites and enstatites (pyroxenes 13 and 49) from South
974 Soufriere Hills Volcano (Montserrat, West Indies) basalts (H_2O, ppm, column 3) and, where
975 melt inclusions could be measured inside them, the water concentration in the melt inclusions
976 (Melt H_2O, wt%, column 2). The partition coefficient for water between augite and melt (equal
977 to 0.003, estimated from a regression through the MI-augite pairs data) yields an estimate of
978 melt H_2O content in column 4.
979

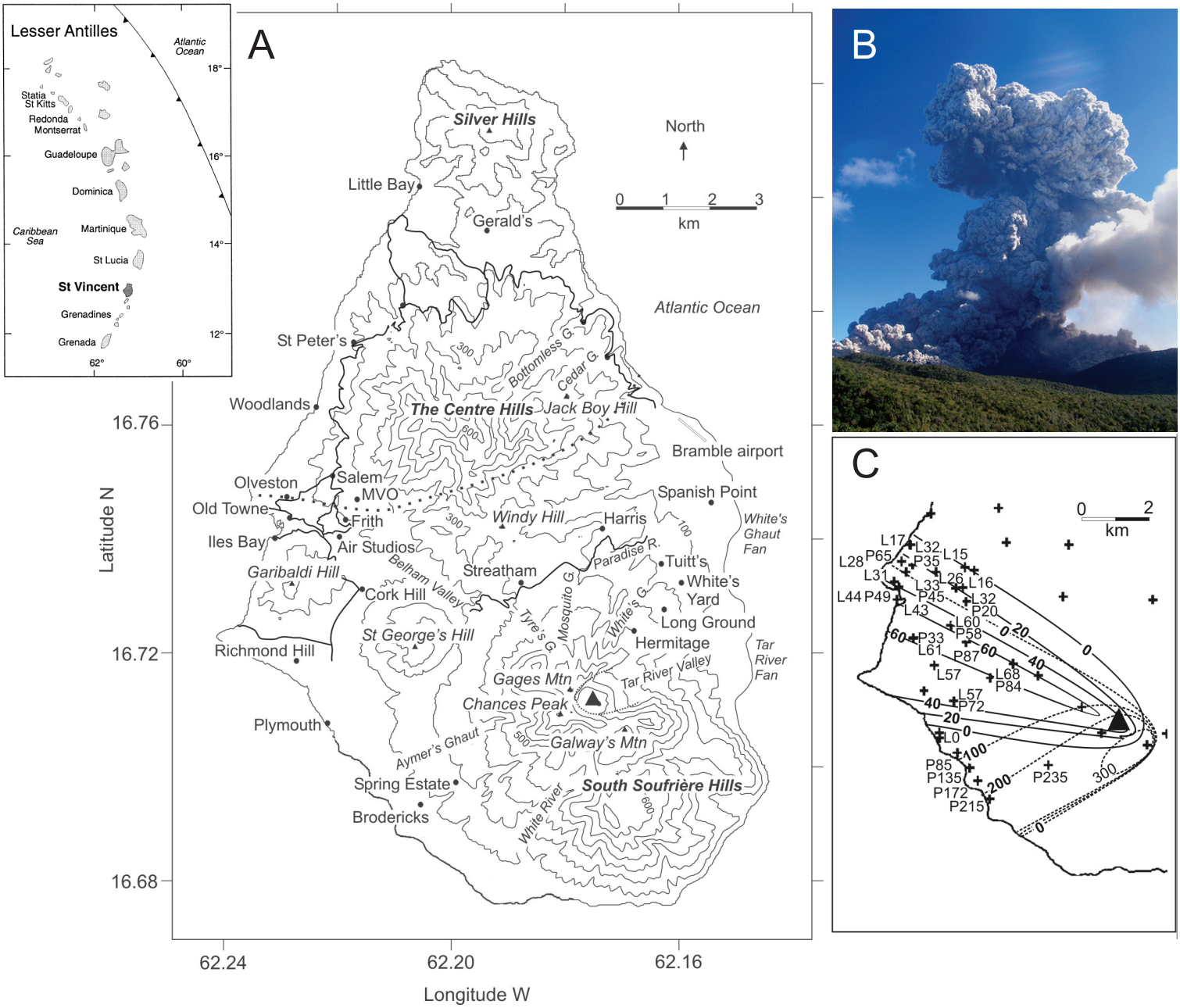
Lesser Antilles
Atlantic Ocean
18°
16°
14°
12°
62°
60°
Statia
St Kitts
Redonda
Montserrat
Guadeloupe
Dominica
Caribbean Sea
Martinique
St Lucia
St Vincent
Grenadines
Grenada
A
Silver Hills
North
0 1 2 3
km
Little Bay
Gerald's
Atlantic Ocean
St Peter's
Bottomless G.
Cedar G.
300
Woodlands
The Centre Hills
Jack Boy Hill
600
Bramble airport
Olveston
Salem
MVO
Old Towne
Frith
Spanish Point
Windy Hill
Harris
White's Ghaut Fan
Iles Bay
Air Studios
100
Paradise R.
Tuitt's
Garibaldi Hill
Belham Valley
Streatham
White's Yard
Cork Hill
Tyre's G.
Mosquito G.
White's G.
Long Ground
St George's Hill
Hermitage
Tar River Fan
Richmond Hill
Gages Mtn
Tar River Valley
Chances Peak
Plymouth
Aymer's Ghaut
500
Galway's Mtn
Spring Estate
South Soufrière Hills
Brodericks
White River
600
16.76
16.72
16.68
Latitude N
62.24
62.20
62.16
Longitude W
B
C
0 2
km
L17
L32
L15
P65
P35
L28
L31
L26
L16
L33
L44
P49
P45
L32
L43
P20
L60
P58
P33
L61
P87
L57
L68
P84
L57
P72
L0
P85
P135
P172
P215
P235
0
20
40
60
100
200
300

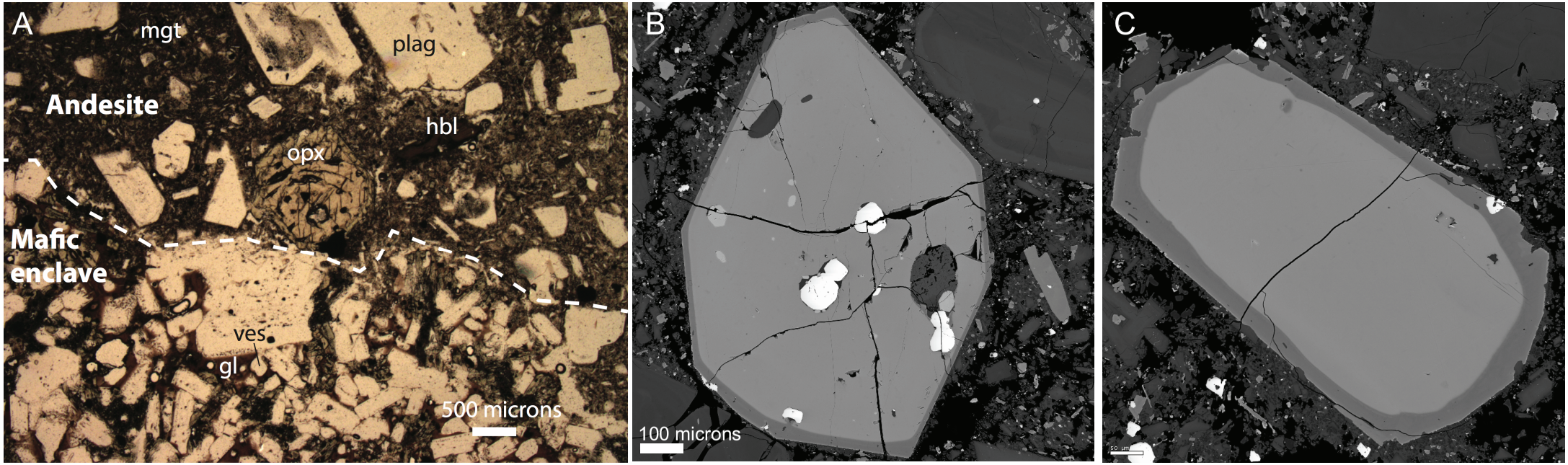
A
mgt
plag
Andesite
hbl
opx
Mafic
enclave
ves
gl
500 microns
B
100 microns
C

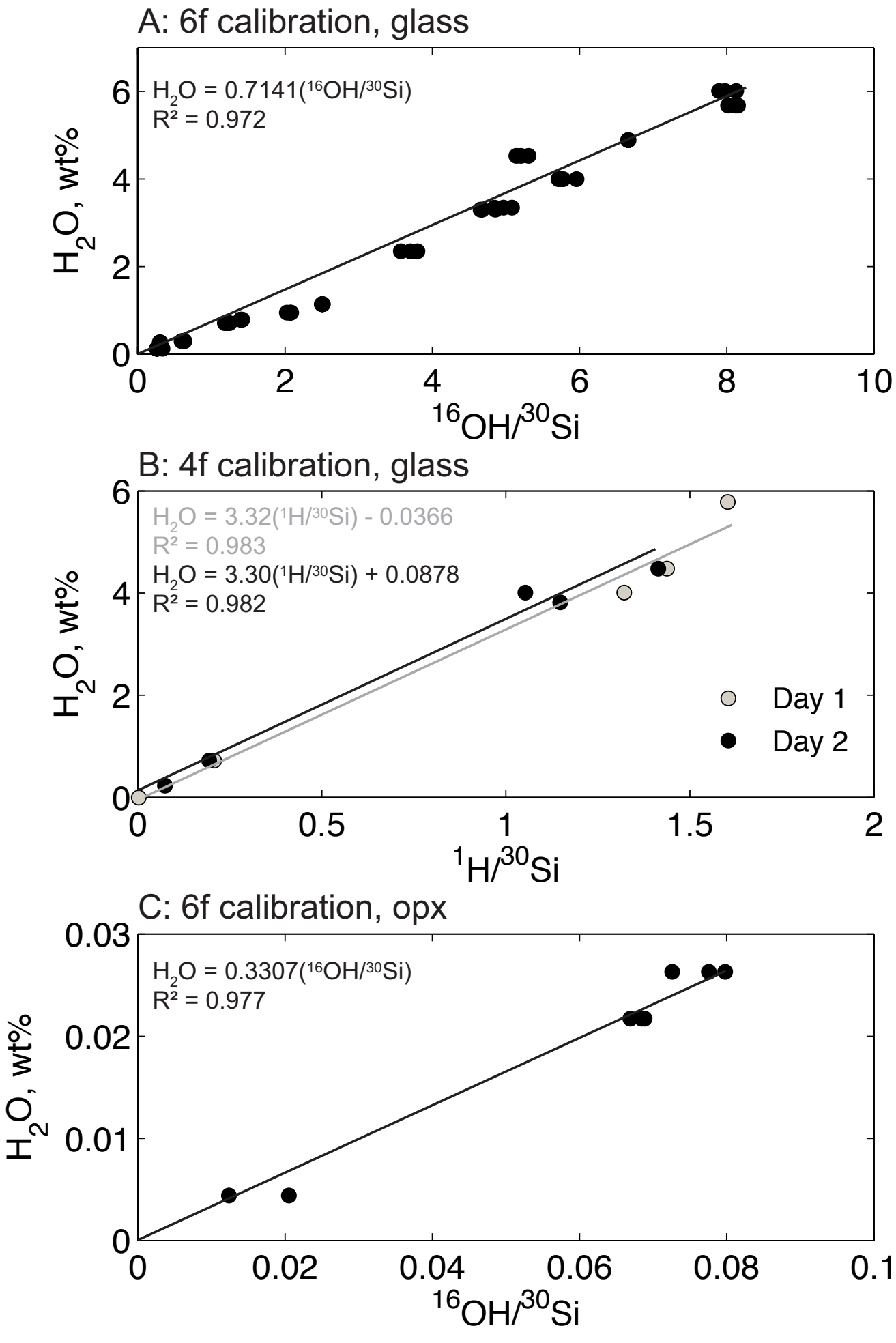
A: 6f calibration, glass
H2O = 0.7141(16OH/30Si)
R² = 0.972
H2O, wt%
16OH/30Si
B: 4f calibration, glass
H2O = 3.32(1H/30Si) - 0.0366
R² = 0.983
H2O = 3.30(1H/30Si) + 0.0878
R² = 0.982
Day 1
Day 2
H2O, wt%
1H/30Si
C: 6f calibration, opx
H2O = 0.3307(16OH/30Si)
R² = 0.977
H2O, wt%
16OH/30Si

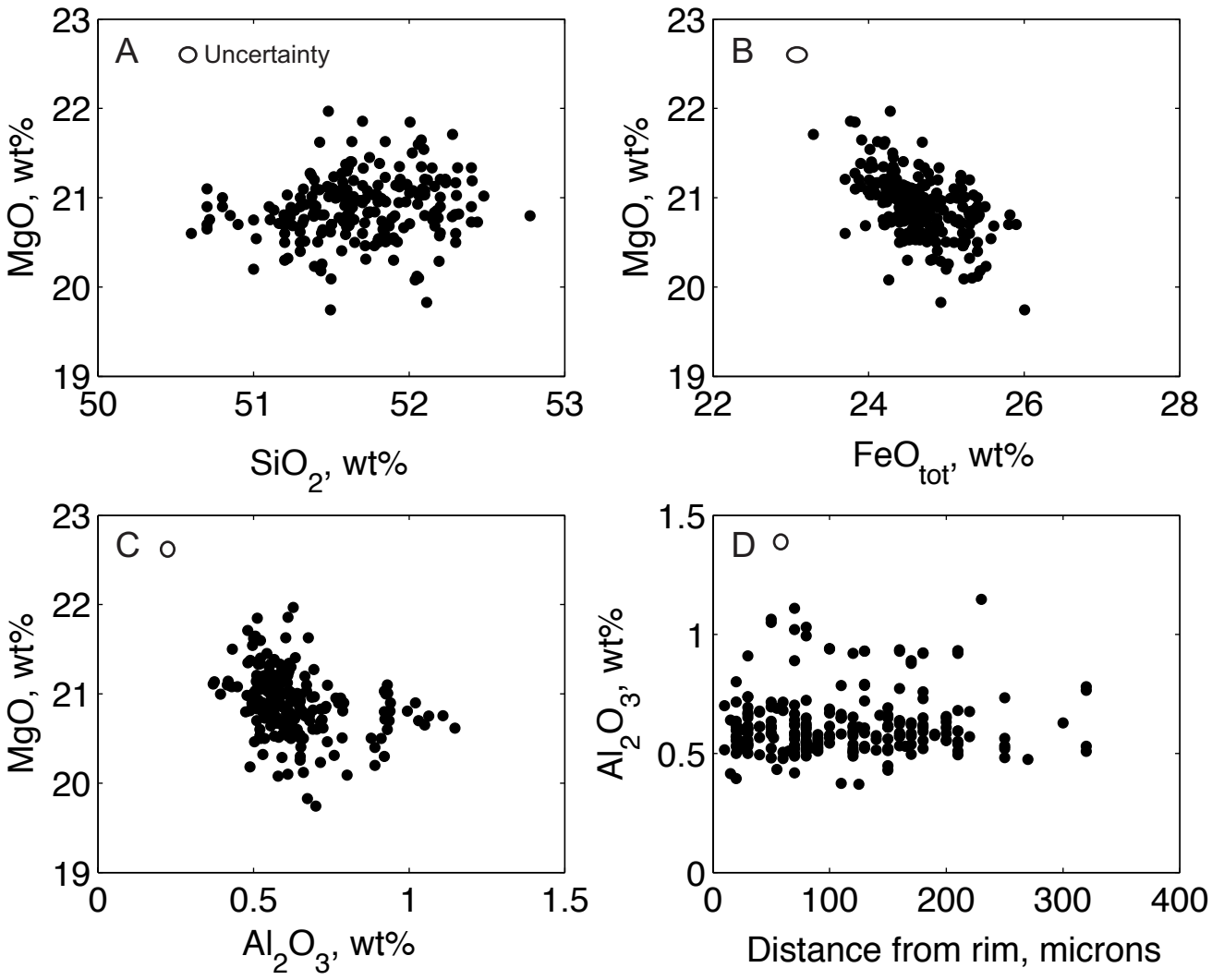
A
Uncertainty
MgO, wt%
SiO2, wt%
B
FeOtot, wt%
C
Al2O3, wt%
D
Al2O3, wt%
Distance from rim, microns

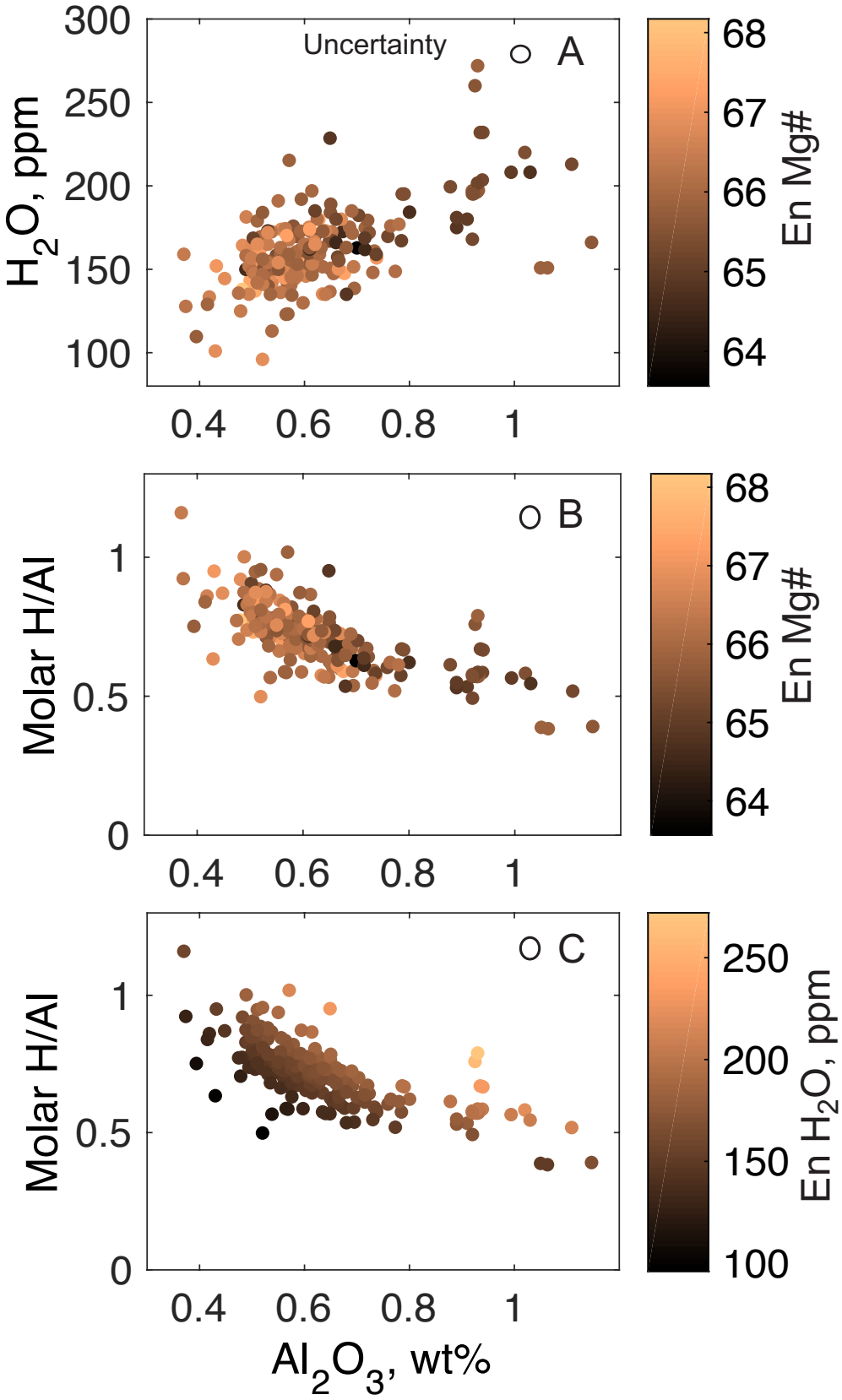
Uncertainty
A
B
C
H_2O, ppm
Molar H/Al
Molar H/Al
Al_2O_3, wt%
En Mg#
En Mg#
En H_2O, ppm
300
250
200
150
100
0.4
0.6
0.8
1
0
0.5
1
68
67
66
65
64
250
200
150
100

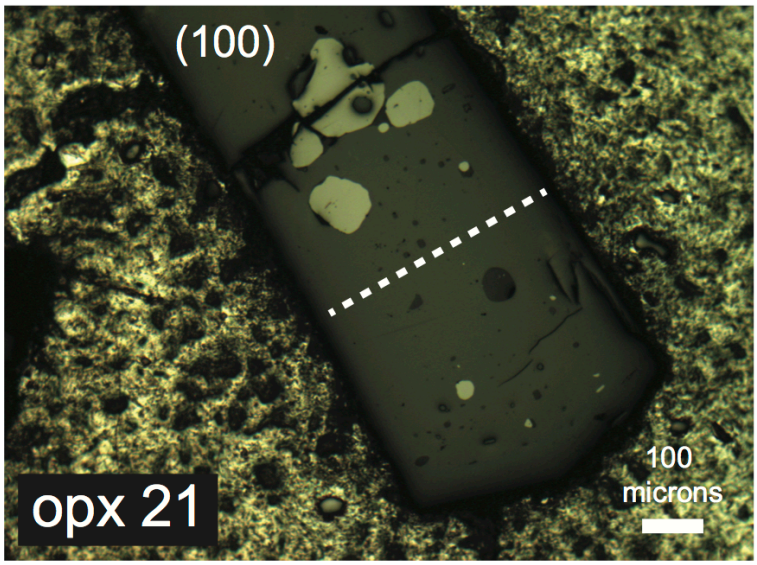
(100)
100
microns
opx 21

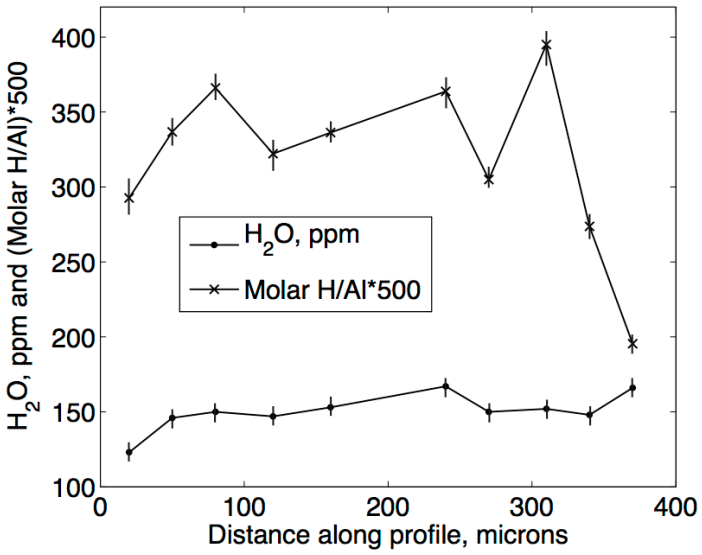
H2O, ppm and (Molar H/Al)*500
H2O, ppm
Molar H/Al*500
Distance along profile, microns

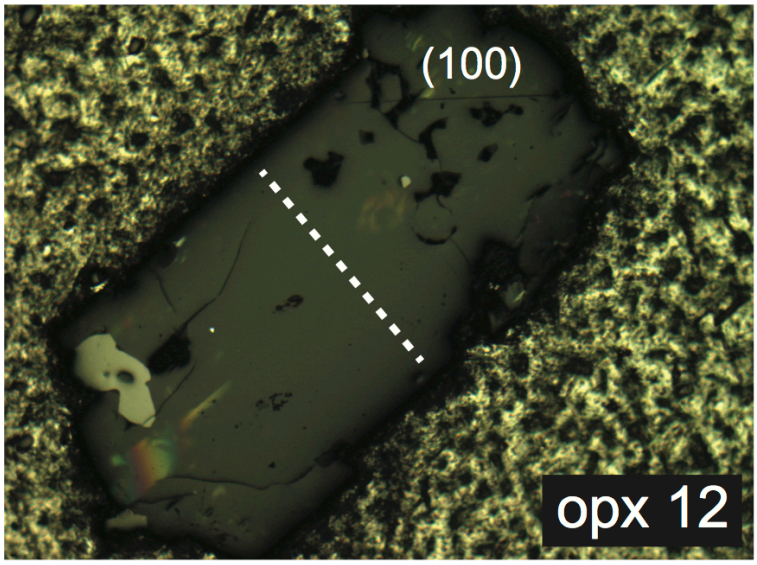
(100)
opx 12

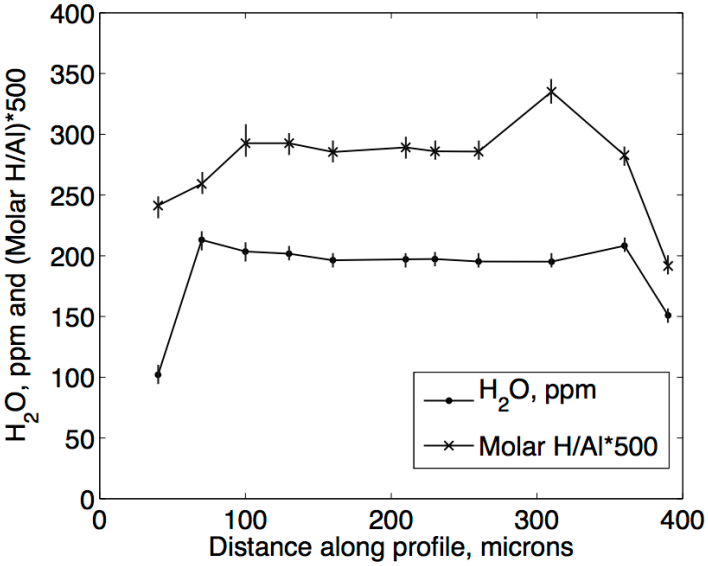
H2O, ppm and (Molar H/Al)*500
H2O, ppm
Molar H/Al*500
Distance along profile, microns

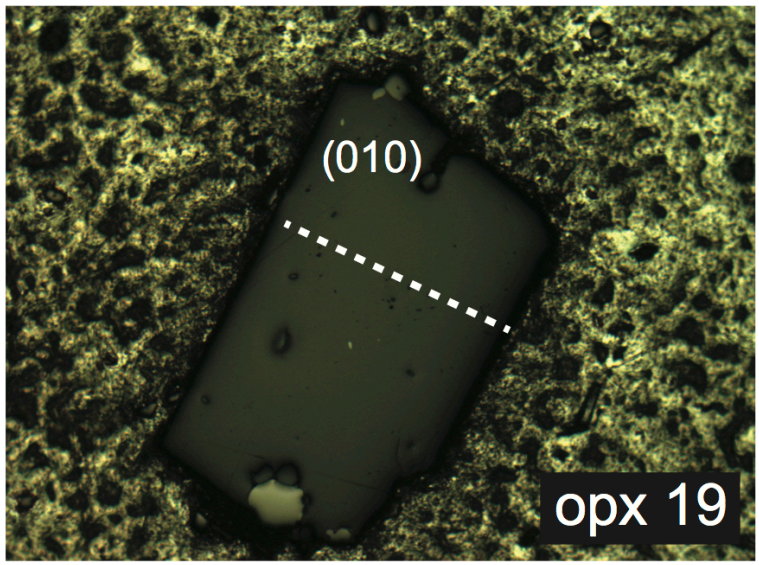
(010)
opx 19

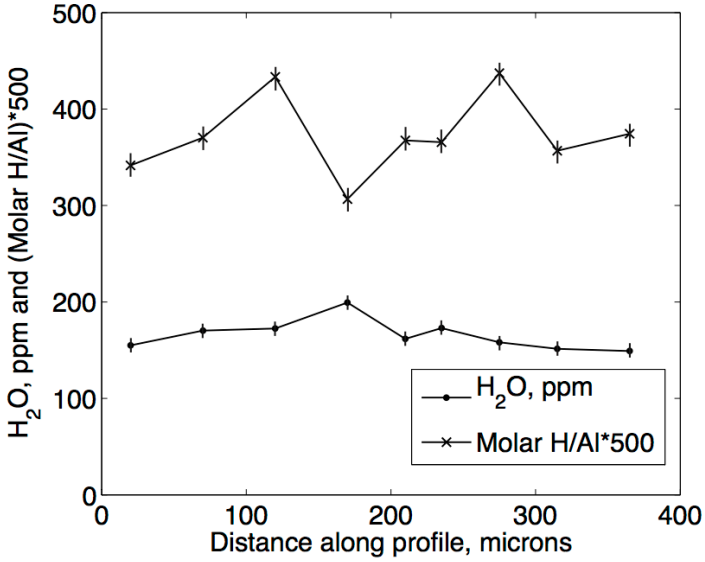
H2O, ppm and (Molar H/Al)*500
H2O, ppm
Molar H/Al*500
Distance along profile, microns

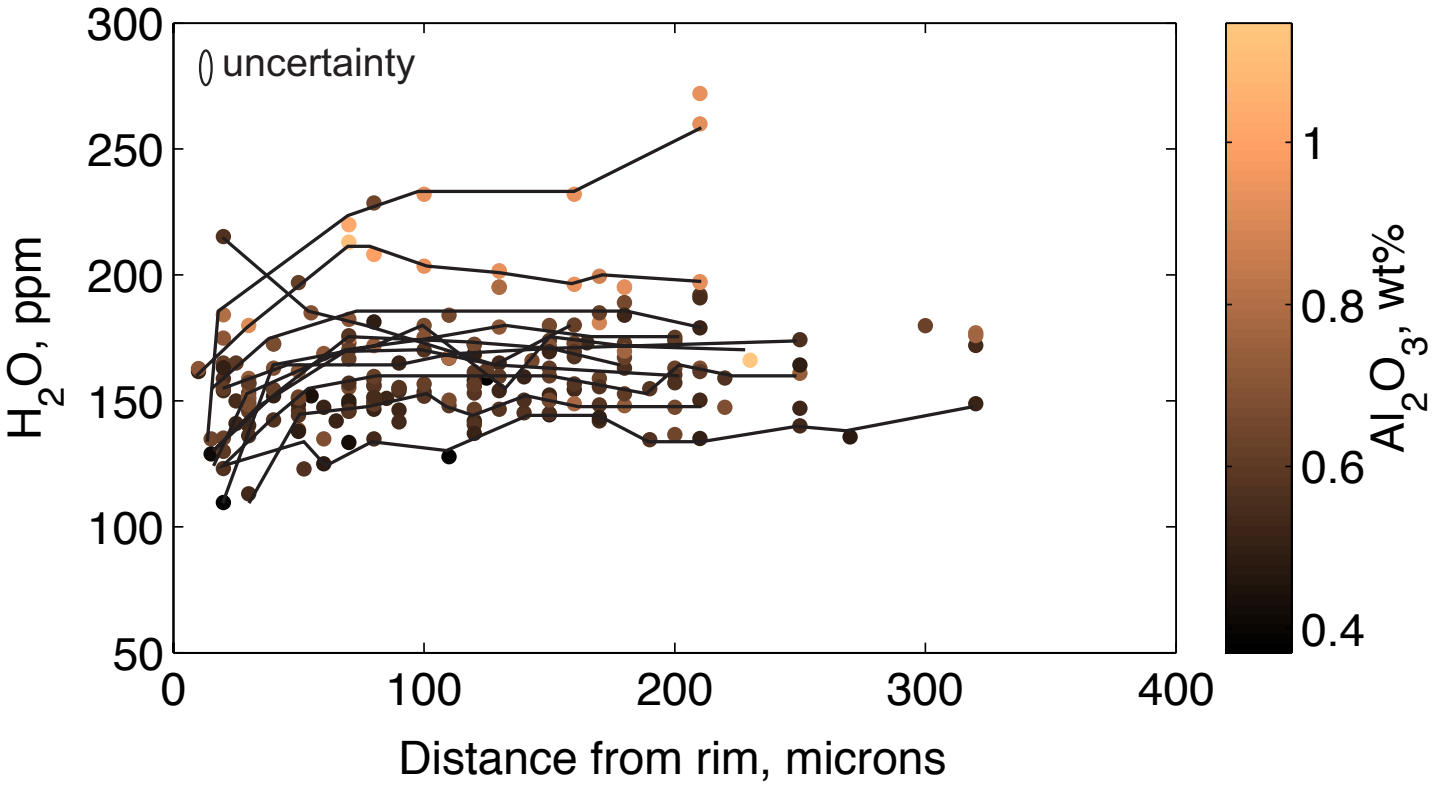
uncertainty
300
250
200
150
100
50
0
100
200
300
400
H2O, ppm
Distance from rim, microns
1
0.8
0.6
0.4
Al2O3, wt%

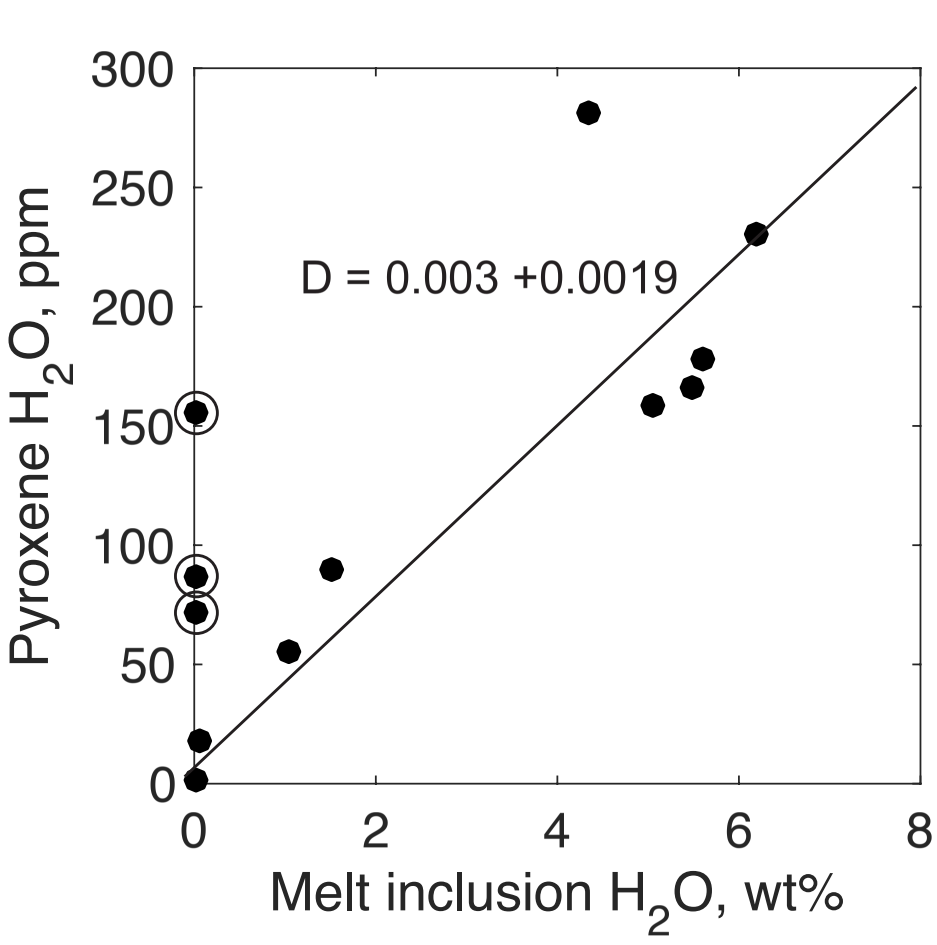
Pyroxene H_2O, ppm
Melt inclusion H_2O, wt%
D = 0.003 +0.0019
0
50
100
150
200
250
300
0
2
4
6
8

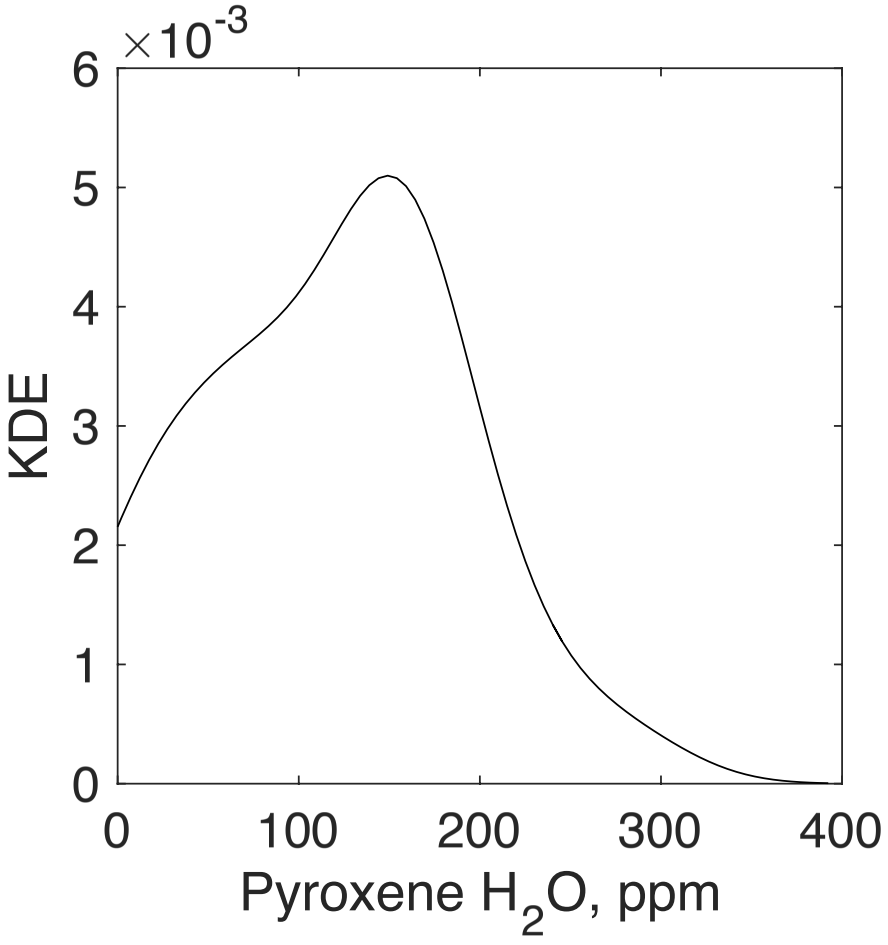
$\times 10^{-3}$
KDE
Pyroxene H_2O, ppm
0
1
2
3
4
5
6
0
100
200
300
400

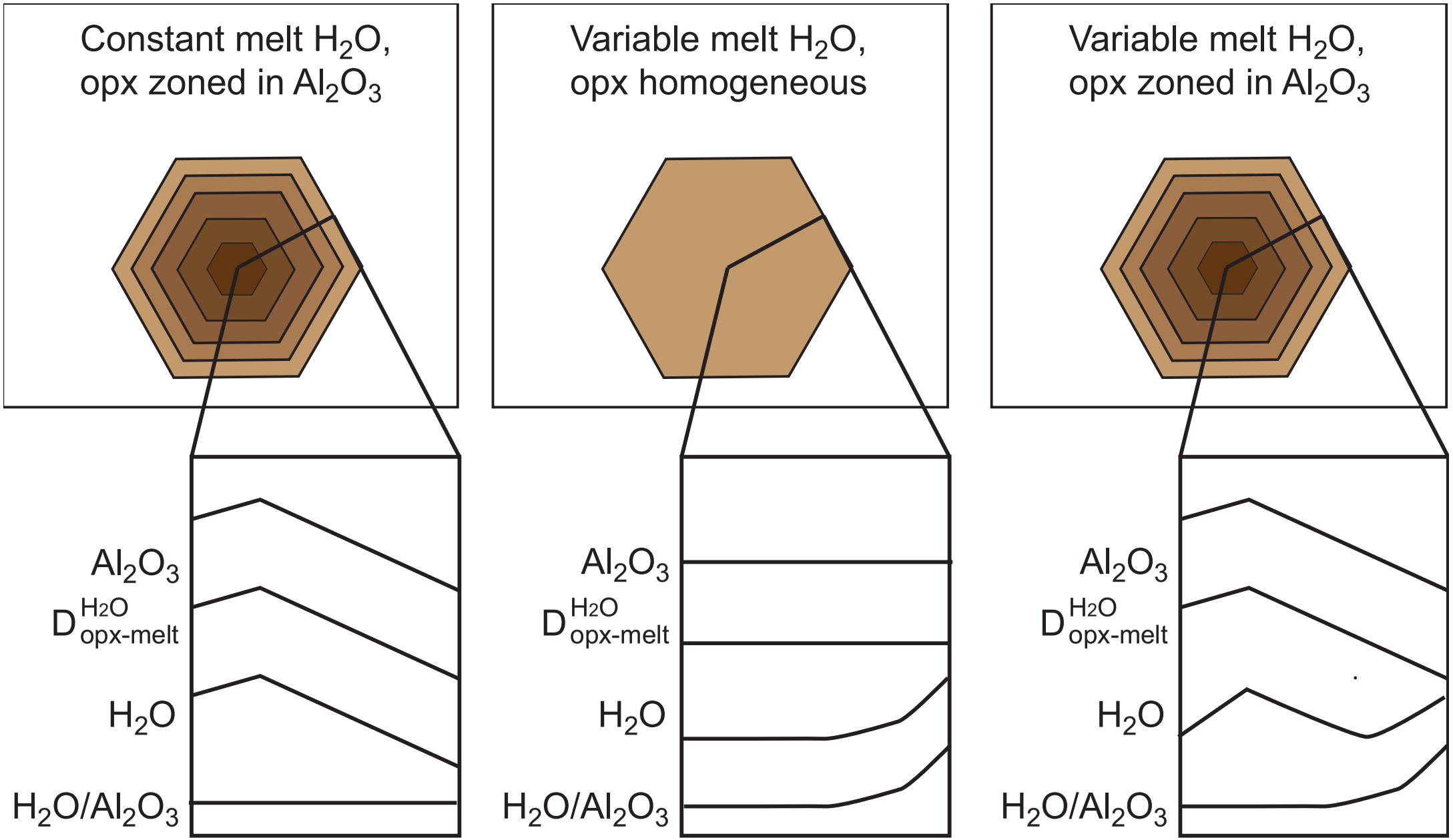
Constant melt H_2O, opx zoned in Al_2O_3
Variable melt H_2O, opx homogeneous
Variable melt H_2O, opx zoned in Al_2O_3
Al_2O_3
$D^{H_2O}_{opx\text{-}melt}$
H_2O
H_2O/Al_2O_3
Al_2O_3
$D^{H_2O}_{opx\text{-}melt}$
H_2O
H_2O/Al_2O_3
Al_2O_3
$D^{H_2O}_{opx\text{-}melt}$
H_2O
H_2O/Al_2O_3

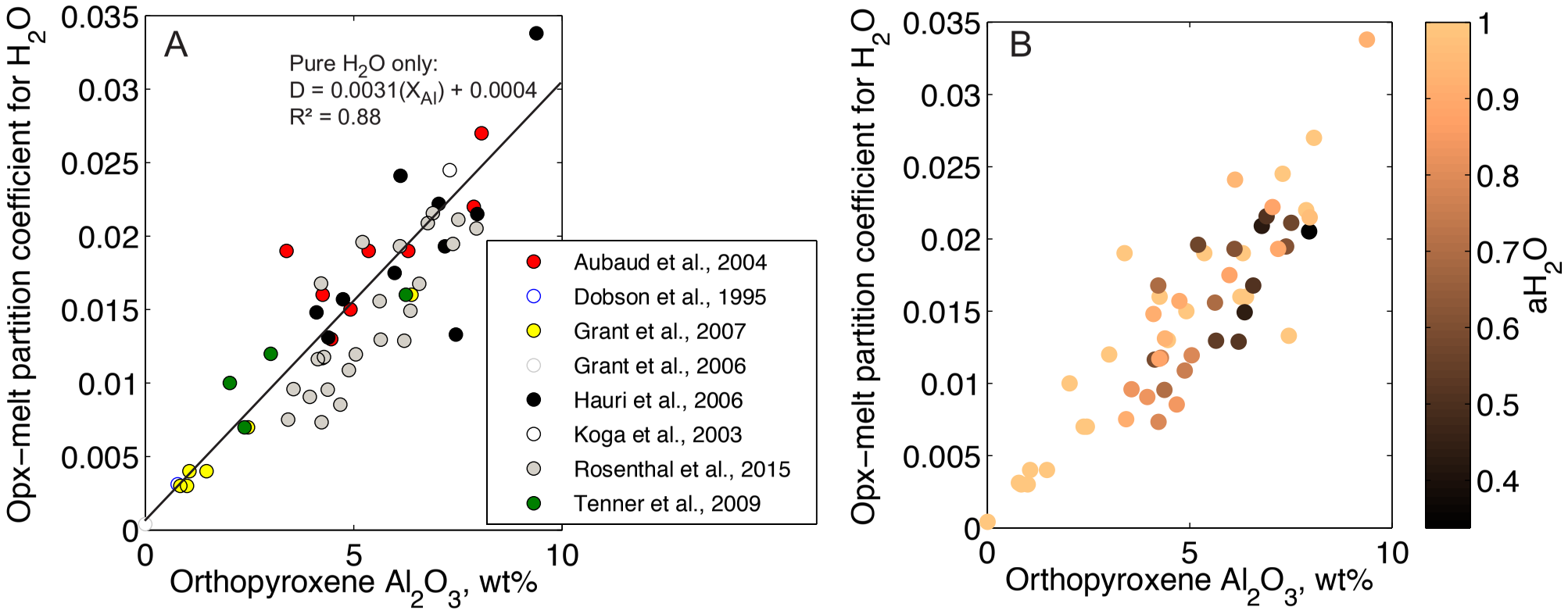
A
Pure H2O only:
D = 0.0031(XAl) + 0.0004
R² = 0.88
Aubaud et al., 2004
Dobson et al., 1995
Grant et al., 2007
Grant et al., 2006
Hauri et al., 2006
Koga et al., 2003
Rosenthal et al., 2015
Tenner et al., 2009
Opx–melt partition coefficient for H2O
Orthopyroxene Al2O3, wt%
0
0.005
0.01
0.015
0.02
0.025
0.03
0.035
0
5
10
B
aH2O
0.4
0.5
0.6
0.7
0.8
0.9
1

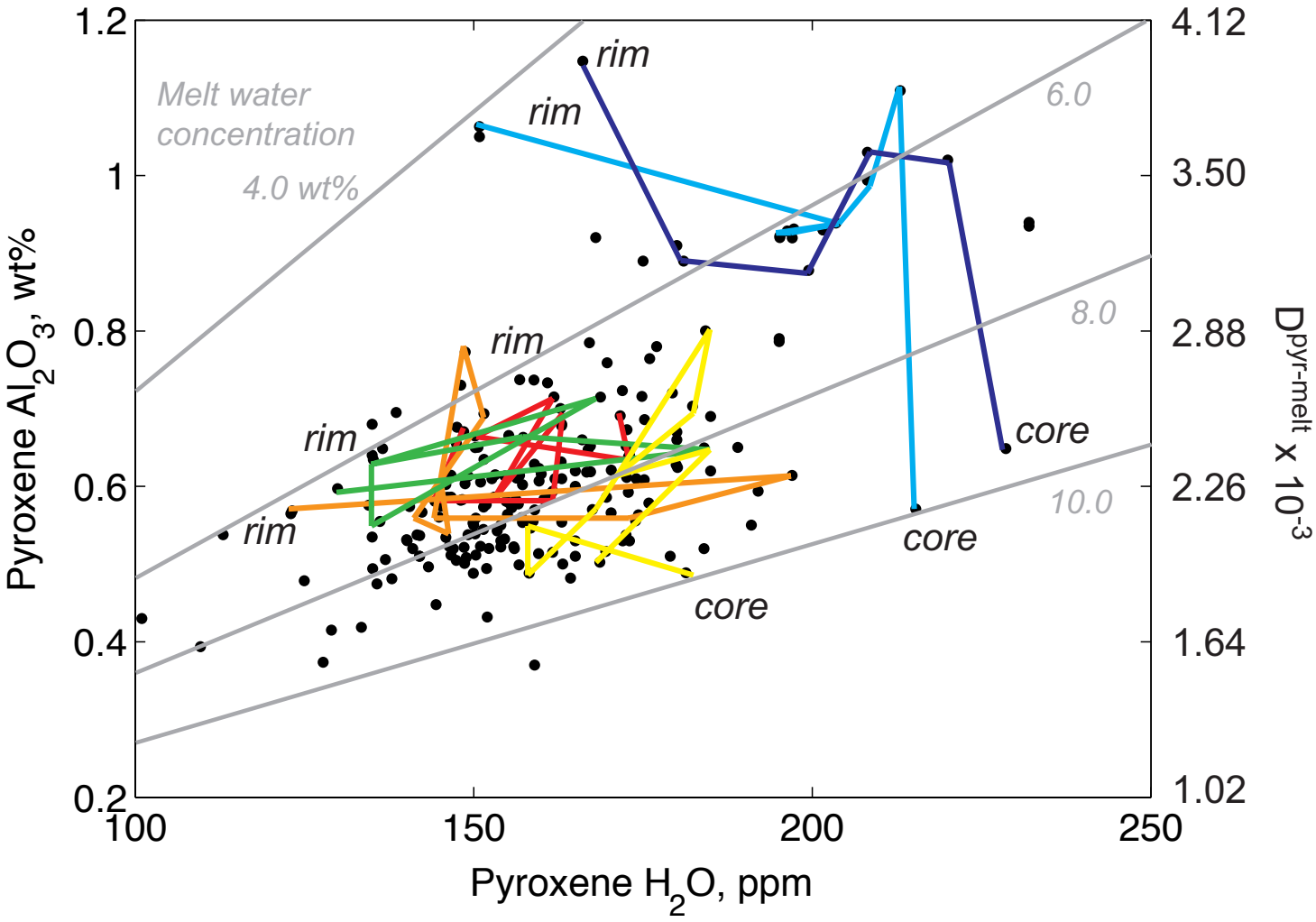
Melt water concentration
4.0 wt%
6.0
8.0
10.0
rim
rim
rim
rim
rim
core
core
core
Pyroxene Al2O3, wt%
Pyroxene H2O, ppm
Dpyr-melt x 10-3
1.2
1
0.8
0.6
0.4
0.2
100
150
200
250
4.12
3.50
2.88
2.26
1.64
1.02

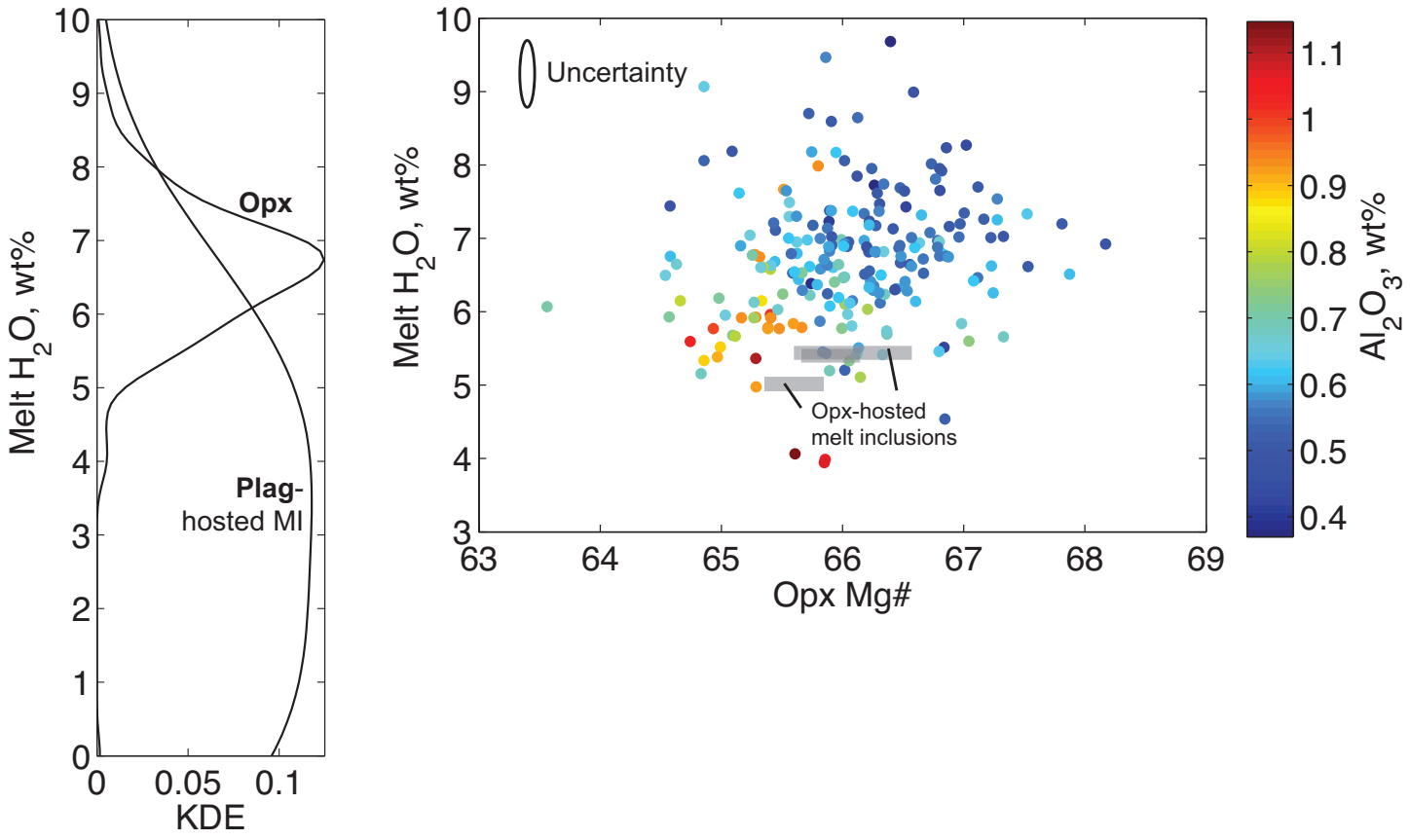
Melt H2O, wt%
10
9
8
7
6
5
4
3
2
1
0
Opx
Plag-
hosted MI
0
0.05
0.1
KDE
Uncertainty
Opx-hosted
melt inclusions
63
64
65
66
67
68
69
Opx Mg#
1.1
1
0.9
0.8
0.7
0.6
0.5
0.4
Al2O3, wt%

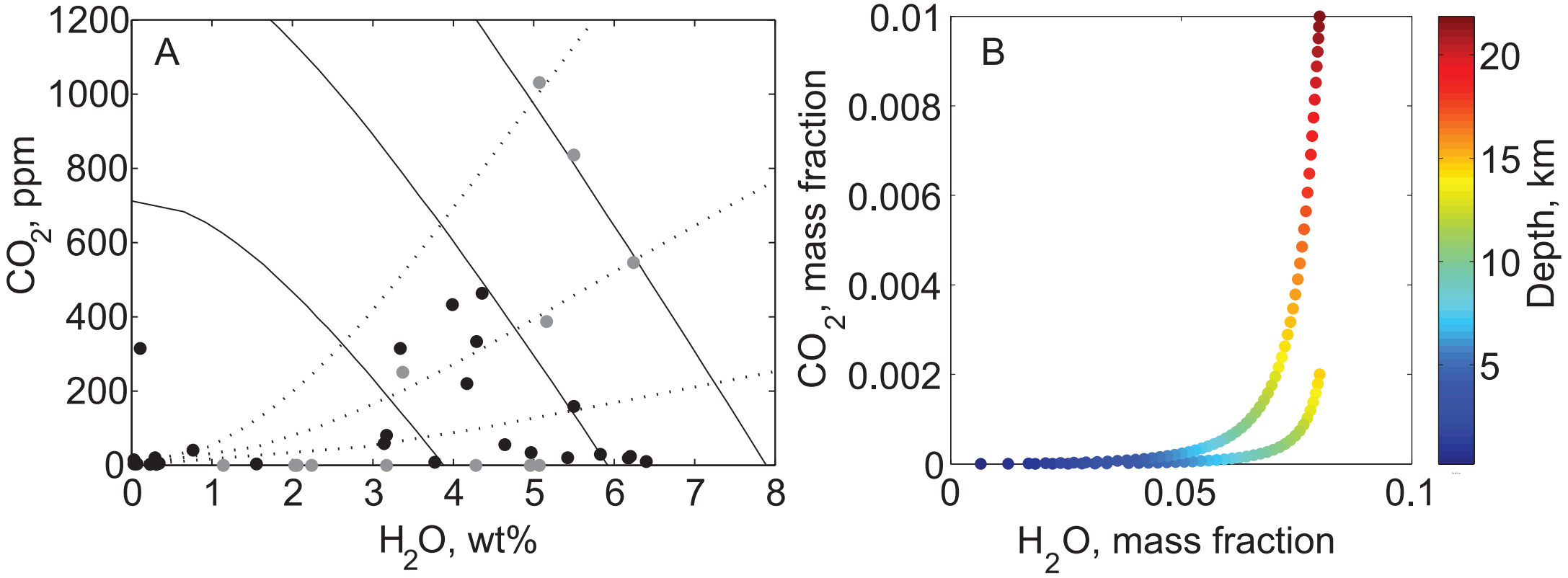
A
1200
1000
800
600
400
200
0
CO_2, ppm
0
1
2
3
4
5
6
7
8
H_2O, wt%
B
0.01
0.008
0.006
0.004
0.002
0
CO_2, mass fraction
0
0.05
0.1
H_2O, mass fraction
20
15
10
5
Depth, km

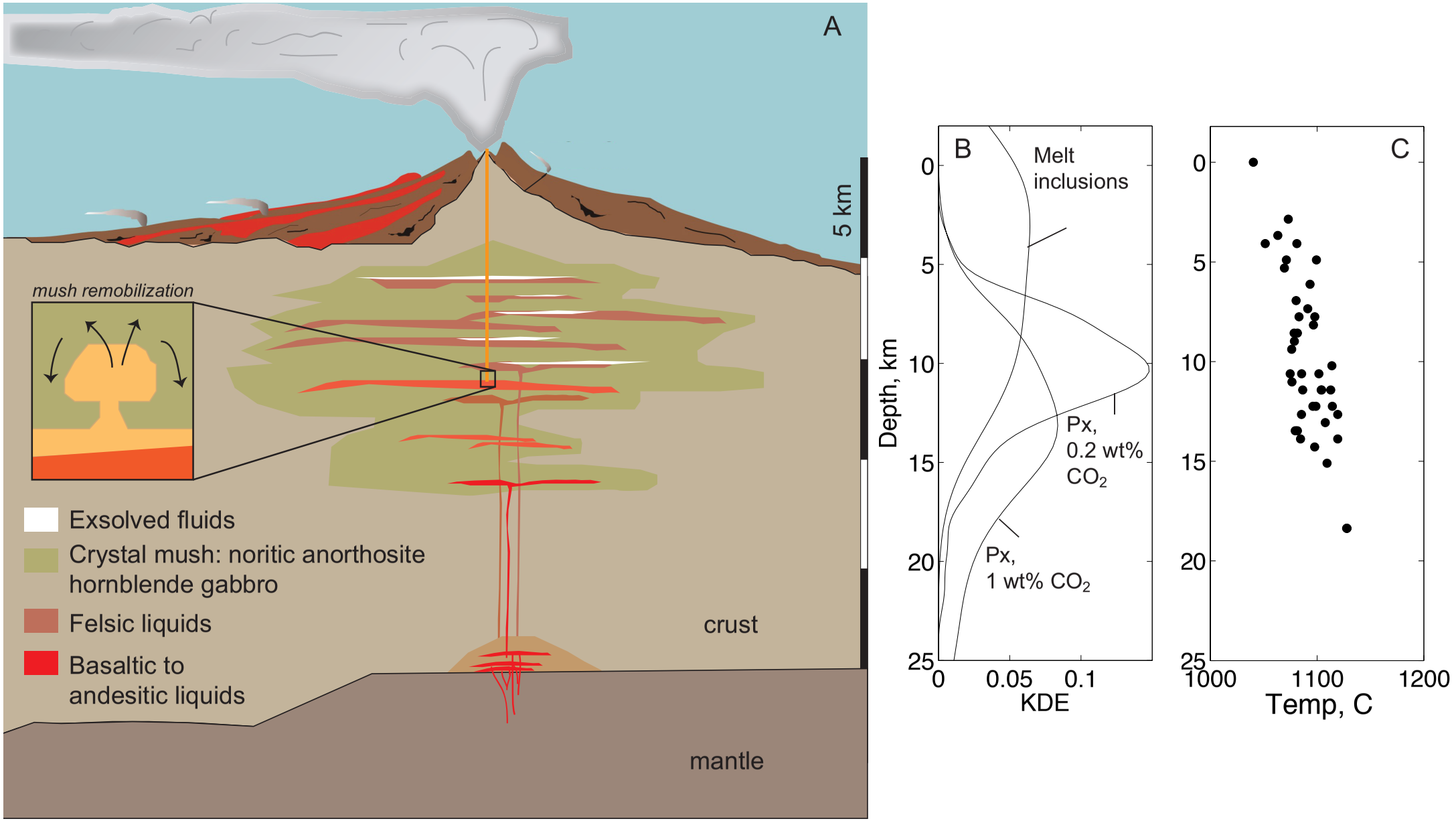
A
5 km
mush remobilization
Exsolved fluids
Crystal mush: noritic anorthosite hornblende gabbro
Felsic liquids
Basaltic to andesitic liquids
crust
mantle
B
Melt inclusions
Px, 0.2 wt% CO_2
Px, 1 wt% CO_2
Depth, km
KDE
C
Temp, C

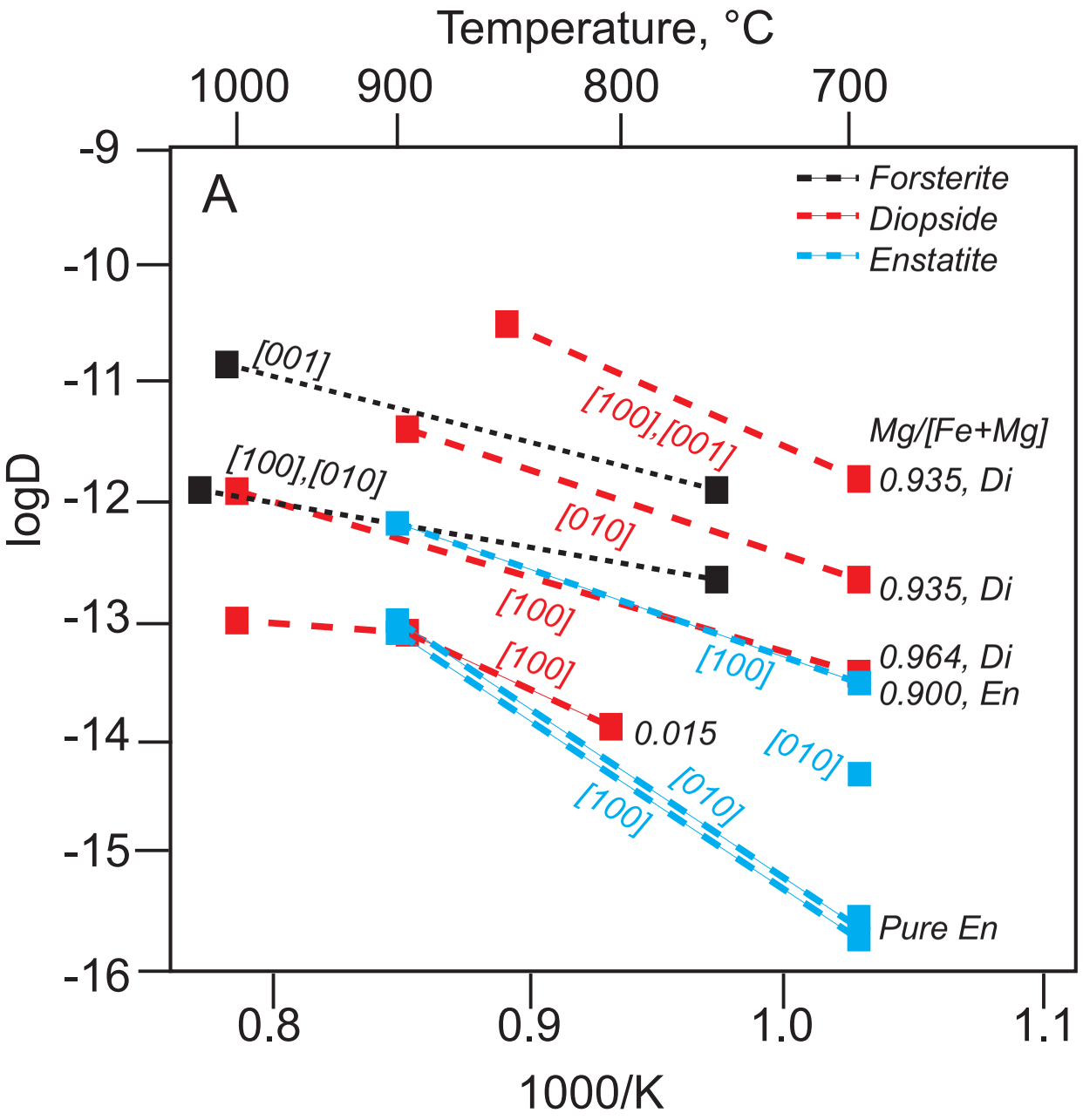
Temperature, °C
1000
900
800
700
A
Forsterite
Diopside
Enstatite
[001]
[100],[001]
[100],[010]
[010]
[100]
[100]
[100]
[010]
[010]
[100]
Mg/[Fe+Mg]
0.935, Di
0.935, Di
0.964, Di
0.900, En
0.015
Pure En
logD
-9
-10
-11
-12
-13
-14
-15
-16
0.8
0.9
1.0
1.1
1000/K

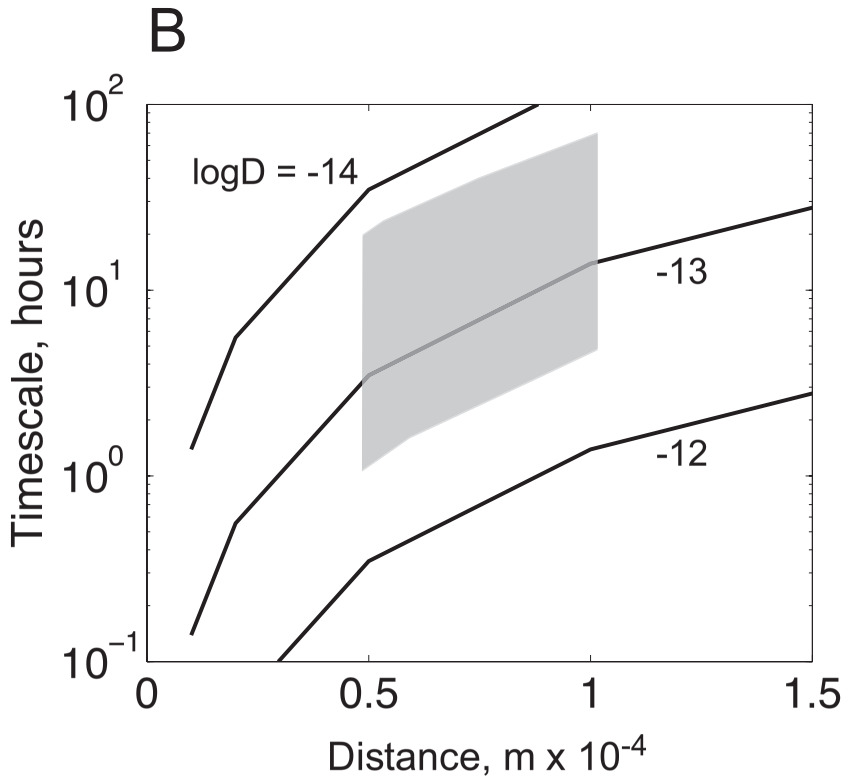
B
logD = -14
-13
-12
Timescale, hours
10^2
10^1
10^0
10^{-1}
0
0.5
1
1.5
Distance, m x 10^{-4}

Analysis no.	SiO_2	Al_2O_3	MnO	FeO	NiO	Na_2O	MgO	Total	Mg #	D	H_2O
1_1	51.9	0.567	1.75	24.7	0.003	0.011	20.5	100.4	65.7	40	142
1_2	51.9	0.785	1.72	25.2	0.004	0.011	20.5	101.2	65.1	110	167
1_3	51.8	0.554	1.70	24.1	0.010	0.037	21.0	100.4	66.7	200	157
1_4	52.0	0.586	1.63	24.9	0.024	0.016	20.7	100.8	65.6	160	170
1_5	52.2	0.623	1.77	25.0	b.d.	0.005	20.8	101.3	65.6	80	160
1_6	52.1	0.585	1.63	24.0	b.d.	0.013	21.3	100.8	67.1	30	
2_1	52.1	0.673	1.69	24.9	b.d.	0.019	19.8	100.2	64.6	40	173
2_2	52.0	0.579	1.58	24.3	b.d.	0.025	20.1	99.7	65.5	70	176
2_3	51.4	0.650	1.53	25.0	b.d.	0.006	20.3	100.0	65.0	150	150
2_4	51.7	0.759	1.81	24.8	0.003	0.018	20.3	100.5	65.3	180	170
2_5	51.3	0.581	1.74	24.4	0.052	0.027	20.5	99.8	65.8	190	155
2_6	51.9	0.578	1.53	24.2	0.041	0.009	20.7	100.1	66.3	160	157
2_7	51.6	0.652	1.56	24.5	0.019	0.032	21.0	100.5	66.3	120	172
2_8	52.1	0.545	1.66	24.4	b.d.	0.022	21.0	100.9	66.5	80	151
2_9	51.4	0.581	1.62	24.6	b.d.	0.033	21.1	100.5	66.3	50	144
2_10	51.5	0.670	1.74	24.6	0.068	0.020	21.1	100.9	66.4	30	149
3_1	51.6	0.613	1.57	24.1	b.d.	0.013	21.3	100.4	67.1	40	155
3_2	52.1	0.560	1.49	24.3	0.054	0.004	21.1	100.8	66.6	70	157
3_3	52.1	0.496	1.60	24.0	b.d.	0.015	21.5	100.9	67.3	170	143
3_4	51.6	0.522	1.48	24.0	b.d.	0.002	21.4	100.2	67.2	130	154
3_5	51.8	0.603	1.41	24.2	0.019	0.011	21.6	100.9	67.2	80	149
3_6	51.6	0.602	1.46	23.8	b.d.	0.002	21.3	99.9	67.2	30	157
4_1	52.1	0.516	1.64	24.8	b.d.	0.012	20.9	100.9	66.0	150	169
4_2	51.9	0.609	1.58	24.3	0.017	0.019	21.1	100.7	66.7	200	175
4_3	52.0	0.570	1.56	24.7	b.d.	0.033	21.1	101.1	66.3	160	168
4_4	52.2	0.612	1.68	24.4	b.d.	0.005	20.8	100.7	66.2	40	173
4_5	51.8	0.686	1.67	24.8	0.000	0.025	21.0	101.2	66.0	100	175
4_6	51.8	0.556	1.66	24.3	0.040	0.017	21.2	100.8	66.8	200	174
4_7	51.6	0.564	1.69	24.5	0.051	0.042	21.0	100.6	66.3	250	174
4_8	51.9	0.482	1.61	24.3	0.042	0.012	21.3	100.8	66.9	250	164
4_9	52.2	0.592	1.64	24.8	0.012	0.013	20.9	101.2	65.9	180	173
4_10	51.6	0.489	1.55	24.6	0.015	0.005	21.4	100.8	66.6	80	181
4_11	51.4	0.500	1.62	24.7	b.d.	0.006	21.6	101.0	66.8	20	163
5_1	52.3	0.481	1.45	23.3	b.d.	0.003	21.7	100.3	68.2	50	138
5_2	52.1	0.506	1.55	23.9	b.d.	0.028	21.6	100.8	67.5	120	137
5_3	51.8	0.566	1.62	23.9	b.d.	0.028	21.4	100.5	67.3	100	170
5_4	51.8	0.478	1.64	24.4	0.021	0.003	21.0	100.4	66.4	60	125
6_1	52.2	0.635	1.46	24.5	b.d.	0.031	20.8	100.7	66.1	50	151
6_2	52.3	0.614	1.57	24.3	0.070	0.020	20.8	100.9	66.3	100	157
6_3	52.3	0.691	1.72	24.6	0.033	0.010	20.8	101.4	66.0	150	172
6_4	51.6	0.652	1.60	24.9	0.003	0.013	20.4	100.2	65.3	110	167
6_5	51.6	0.678	1.63	24.2	b.d.	0.039	20.8	100.1	66.3	40	163
7_1	51.8	0.583	1.68	24.2	b.d.	0.003	21.0	100.5	66.5	170	148
7_2	51.6	0.577	1.55	24.2	0.044	0.024	21.0	100.2	66.6	100	152
7_3	51.2	0.663	1.79	25.4	0.051	0.005	20.8	101.0	65.3	30	157
8_1	51.5	0.628	1.41	24.3	0.007	0.002	22.0	100.7	67.5	300	180
8_2	51.6	0.676	1.46	24.1	b.d.	0.010	21.6	100.6	67.3	220	148
8_3	52.0	0.512	1.46	23.8	0.016	0.014	21.8	100.8	67.8	150	150
8_4	51.7	0.611	1.33	23.8	b.d.	0.025	21.9	100.4	67.9	120	156
9_1	51.4	0.694	1.63	24.8	0.024	0.003	21.3	100.9	66.4	30	151
9_2	51.4	0.613	1.60	25.2	b.d.	0.006	21.2	101.1	66.0	80	149

8_3	52.0	0.512	1.46	23.8	0.010	0.014	21.8	100.8	67.8	150	150
8_4	51.7	0.611	1.33	23.8	b.d.	0.025	21.9	100.4	67.9	120	156
9_1	51.4	0.694	1.63	24.8	0.024	0.003	21.3	100.9	66.4	30	151
9_2	51.4	0.613	1.60	25.2	b.d.	0.006	21.2	101.1	66.0	80	149
9_4	51.5	0.586	1.54	24.3	0.002	0.023	21.0	100.0	66.5	70	146
9_5	51.5	0.606	1.64	24.4	0.032	0.023	20.8	100.1	66.2	50	151
9_6	51.7	0.716	1.62	24.7	b.d.	0.003	20.8	100.8	65.9	20	175
9_7	51.5	0.700	1.66	26.0	b.d.	0.042	19.7	99.7	63.6	10	163
10_1	51.3	0.650	1.57	24.7	b.d.	0.001	20.9	100.3	66.0	30	151
10_2	51.3	0.723	1.73	24.9	0.002	0.005	20.6	100.4	65.5	80	172
10_3	51.5	0.514	1.53	24.7	0.008	0.016	21.1	100.4	66.3	140	160
10_4	51.4	0.619	1.65	24.7	b.d.	0.010	20.9	100.4	66.0	180	167
10_5	51.2	0.720	1.55	24.9	b.d.	0.015	20.7	100.1	65.7	130	179
10_6	51.7	0.579	1.58	24.0	0.016	0.010	21.1	100.1	66.9	90	155
10_7	52.1	0.522	1.45	24.2	0.009	0.026	21.6	101.0	67.2	50	149
10_8	51.3	0.737	1.41	23.8	0.000	0.022	21.1	99.6	67.0	30	157
10_9	51.7	0.515	1.45	24.0	b.d.	0.022	21.3	100.2	67.1	10	162
12_1	51.6	0.571	1.77	24.9	b.d.	0.018	20.9	100.8	65.9	20	102
12_2	50.7	1.109	1.51	25.4	0.013	0.025	20.8	100.1	65.3	70	213
12_3	51.4	0.939	1.61	25.4	b.d.	0.023	20.8	100.9	65.3	100	203
12_4	51.2	0.930	1.56	25.2	0.030	0.012	20.7	100.2	65.4	130	202
12_5	51.6	0.929	1.47	25.1	b.d.	0.029	20.7	100.5	65.5	160	196
12_6	51.2	0.920	1.51	25.3	0.047	0.004	21.0	100.8	65.6	210	197
12_7	51.5	0.931	1.47	25.2	0.001	0.010	21.0	100.9	65.7	210	197
12_8	51.3	0.922	1.63	25.2	0.043	0.008	20.7	100.5	65.4	180	195
12_9	51.4	0.786	1.67	25.4	0.043	0.025	20.8	100.7	65.3	130	195
12_10	51.2	0.994	1.58	25.8	0.017	0.011	20.8	101.1	64.9	80	208
12_11	51.0	1.063	1.57	24.7	0.020	0.005	20.8	99.9	65.8	50	151
15_1	51.6	0.597	1.48	24.7	0.014	0.003	21.0	100.6	66.1	20	130
15_2	51.6	0.614	1.49	24.4	0.018	0.003	20.6	99.8	65.9	50	197
15_3	51.3	0.583	1.71	24.0	0.016	0.007	20.7	99.3	66.5	80	156
15_4	51.8	0.574	1.65	24.5	0.060	0.012	20.7	100.3	66.1	120	141
15_5	51.6	0.773	1.74	24.6	0.065	0.022	20.9	100.8	66.1	160	149
15_6	51.5	0.655	1.57	24.5	0.020	0.006	20.8	100.1	66.1	200	147
15_7	51.2	0.733	1.65	24.7	0.020	0.020	20.9	100.2	66.0	250	161
15_8	51.5	0.586	1.59	24.6	0.009	0.021	21.2	100.7	66.4	130	147
15_9	51.5	0.522	1.61	23.9	0.008	0.006	21.1	99.6	67.0	80	156
15_10	51.4	0.603	1.59	24.2	0.027	0.000	21.0	99.9	66.6	30	146
17_1	51.5	0.800	1.75	25.2	0.037	0.013	20.1	100.3	64.7	20	184
17_2	51.4	0.715	1.65	25.5	0.022	0.026	20.2	100.4	64.6	50	162
17_3	51.7	0.546	1.66	25.3	0.005	0.004	20.8	101.1	65.4	80	158
17_4	51.3	0.648	1.69	25.3	0.015	0.013	20.9	100.7	65.4	110	167
17_5	51.0	0.649	1.80	25.6	0.023	0.003	20.5	100.5	64.9	80	229
18_1	51.7	0.737	1.65	25.2	-0.022	-0.002	20.5	100.9	65.1	30	159
18_2	51.4	0.488	1.55	25.4	0.024	0.018	20.2	100.1	64.6	70	150
18_3	52.2	0.591	1.53	24.9	0.028	0.002	20.3	100.6	65.2	120	161
18_4	52.2	0.560	1.56	23.9	0.032	0.017	21.2	100.7	67.1	150	145
18_5	51.8	0.610	1.62	24.5	0.018	0.005	20.5	100.2	65.8	180	153
18_6	52.4	0.537	1.55	24.3	0.057	0.011	20.7	100.6	66.2	170	142
18_7	51.8	0.502	1.58	25.2	0.019	0.000	20.5	100.7	65.1	120	169
18_8	51.9	0.538	1.56	24.4	0.003	0.015	21.2	100.7	66.7	90	142
18_9	51.9	0.715	1.63	25.6	0.036	0.026	20.7	101.5	65.0	60	169
19_1	51.8	0.613	1.65	24.7	0.061	0.019	20.5	100.5	65.6	20	155
19_2	52.2	0.621	1.56	24.8	0.029	0.014	20.6	101.0	65.6	70	170
19_3	51.8	0.537	1.62	24.4	0.012	0.006	20.8	100.4	66.2	120	172
19_4	51.4	0.878	1.59	25.0	0.042	0.021	20.5	100.6	65.3	170	199
19_5	51.8	0.594	1.60	24.6	0.068	0.003	20.6	100.4	65.9	210	162
19_6	51.8	0.638	1.62	24.8	0.033	0.014	20.6	100.6	65.6	160	173
19_7	52.3	0.489	1.61	24.5	0.033	0.026	20.8	100.9	66.1	120	158
19_8	52.2	0.573	1.54	24.6	0.020	0.014	20.7	100.7	65.9	80	151

19_6	51.8	0.638	1.62	24.8	0.033	0.014	20.6	100.6	65.6	160	173
19_7	52.3	0.489	1.61	24.5	0.033	0.026	20.8	100.9	66.1	120	158
19_8	52.2	0.573	1.54	24.6	0.020	0.014	20.7	100.7	65.9	80	151
19_9	52.2	0.538	1.57	24.5	0.027	0.018	21.1	101.0	66.5	30	149
21_2	52.0	0.568	1.58	24.7	0.020	0.035	20.7	100.7	65.9	20	123
21_3	52.4	0.586	1.51	24.8	0.005	0.001	21.2	101.7	66.3	50	146
21_4	51.6	0.553	1.57	24.2	0.030	0.007	21.2	100.2	66.8	80	150
21_5	51.9	0.614	1.62	24.7	0.013	0.000	20.8	100.8	65.9	120	147
21_6	52.3	0.615	1.48	24.3	0.085	0.028	21.0	100.9	66.5	160	153
21_7	52.5	0.619	1.62	24.2	0.068	0.011	21.0	101.1	66.6	160	167
21_8	52.2	0.665	1.46	24.0	0.012	0.035	21.2	100.8	67.0	130	150
21_9	52.1	0.520	1.37	24.2	0.051	0.004	21.3	100.6	67.0	90	152
21_10	51.7	0.730	1.49	24.6	0.009	0.011	20.8	100.7	66.1	60	148
21_11	51.5	1.147	1.52	24.8	0.019	0.030	20.6	101.0	65.6	20	166
22_1	52.3	0.555	1.35	24.9	0.026	0.016	21.3	101.5	66.3	30	136
22_2	52.1	0.564	1.41	24.0	0.065	0.003	21.0	100.2	66.8	90	155
22_3	51.6	0.559	1.62	24.2	0.004	0.012	21.1	100.1	66.7	140	150
22_4	51.9	0.494	1.39	24.2	0.025	0.004	20.9	100.0	66.6	210	135
22_5	52.8	0.475	1.44	24.4	0.005	0.013	20.8	100.9	66.2	270	136
22_6	51.9	0.508	1.35	24.1	0.043	0.002	21.1	99.9	66.9	320	149
22_7	52.0	0.765	1.51	24.8	0.058	0.028	21.0	100.8	66.0	320	176
22_8	52.1	0.531	1.59	24.9	0.016	0.025	21.2	101.2	66.2	250	140
22_9	52.0	0.448	1.47	24.1	0.000	0.017	21.1	100.1	66.8	150	144
22_10	52.2	0.534	1.35	24.1	0.054	0.016	21.2	100.5	66.9	70	146
25_1	51.6	0.494	1.47	24.4	0.006	0.009	20.9	100.0	66.3	40	152
25_2	51.4	0.703	1.76	25.2	0.059	0.011	20.6	100.8	65.3	70	182
25_3	51.8	0.649	1.60	24.8	0.033	0.004	20.5	100.5	65.6	110	184
25_4	51.3	0.624	1.63	24.5	0.054	0.001	20.8	100.0	66.1	160	180
25_5	51.6	0.616	1.66	24.8	0.063	0.038	20.7	100.6	65.7	150	160
25_6	51.7	0.543	1.66	24.3	0.028	0.023	21.5	100.9	67.0	100	153
25_7	51.4	0.501	1.57	24.4	0.029	0.008	20.9	99.9	66.2	70	149
25_8	51.5	0.499	1.47	24.3	0.086	0.022	21.0	100.0	66.5	30	157
27_4	51.6	0.634	1.38	24.4	0.027	0.005	21.4	100.7	66.8	20	135
27_5	51.7	0.695	1.61	24.9	0.056	0.019	21.0	101.1	65.9	50	139
27_6	52.2	0.512	1.57	24.8	0.031	0.010	20.8	100.9	65.9	80	147
27_7	51.7	0.582	1.61	24.6	0.025	0.020	21.0	100.7	66.2	110	148
27_8	51.6	0.574	1.64	24.6	0.072	0.002	21.0	100.6	66.3	140	145
27_9	51.6	0.573	1.80	24.6	0.027	0.005	20.7	100.4	65.9	170	156
27_10	51.6	0.649	1.51	24.6	0.001	0.004	20.9	100.4	66.1	200	137
27_11	51.8	0.576	1.72	25.1	0.023	0.007	21.0	101.3	65.8	190	134
27_12	51.2	0.586	1.72	24.9	0.004	0.018	20.9	100.5	65.8	120	153
27_13	51.1	0.666	1.59	25.2	0.009	0.018	20.8	100.4	65.5	70	155
28_1	51.4	0.555	1.71	24.6	0.031	0.012	20.6	100.1	65.9	20	159
28_2	51.8	0.505	1.52	24.4	0.023	0.001	21.0	100.3	66.4	60	147
28_3	52.0	0.523	1.75	24.9	0.007	0.032	21.1	101.4	66.0	90	146
28_4	51.6	0.607	1.57	25.3	0.030	0.009	20.8	101.1	65.4	130	160
28_5	51.4	0.629	1.72	24.8	0.014	0.038	20.9	100.6	66.0	170	159
28_6	51.6	0.584	1.66	24.8	0.040	0.031	21.0	100.9	66.0	200	160
28_7	51.7	0.632	1.72	24.6	0.007	0.022	20.7	100.6	65.9	200	163
28_8	51.6	0.539	1.65	25.2	0.038	0.017	21.2	101.4	65.9	210	150
28_9	51.1	0.532	1.60	25.0	0.041	0.025	20.9	100.2	65.8	160	155
28_10	51.7	0.374	1.56	24.7	0.029	0.007	21.1	100.7	66.3	110	128
28_11	52.0	0.419	1.59	24.4	0.012	0.013	21.1	100.7	66.5	70	133
28_12	51.4	0.530	1.71	25.1	0.034	0.011	20.8	100.6	65.6	30	140
28_13	51.5	0.394	1.74	25.1	0.033	0.009	21.0	100.9	65.7	20	110
29_1	51.3	0.600	1.51	24.7	0.020	0.011	21.0	100.1	66.2	25	165
29_2	51.7	0.523	1.71	24.9	0.003	0.029	20.5	100.4	65.4	85	151
29_3	52.1	0.610	1.36	25.3	0.032	0.002	20.1	100.6	64.6	125	162
29_4	52.1	0.660	1.62	25.4	0.009	0.027	20.1	101.0	64.5	143	166

29_2	51.7	0.523	1.71	24.9	0.003	0.029	20.5	100.4	65.4	85	151
29_3	52.1	0.610	1.36	25.3	0.032	0.002	20.1	100.6	64.6	125	162
29_4	52.1	0.660	1.62	25.4	0.009	0.027	20.1	101.0	64.5	143	166
29_5	51.6	0.554	1.25	24.7	0.030	0.020	21.0	100.2	66.2	180	163
29_6	51.9	0.680	1.44	24.9	0.006	0.011	20.8	100.8	65.7	210	163
29_7	51.4	0.570	1.23	25.3	0.032	0.009	21.2	100.9	65.8	220	159
29_8	51.2	0.530	1.43	25.3	0.043	0.015	20.3	99.9	64.9	165	173
29_9	51.5	0.370	1.36	24.6	0.039	0.017	21.1	100.9	66.4	125	159
29_10	52.0	0.432	1.53	24.3	0.022	0.010	21.5	100.9	67.0	55	152
29_11	51.4	0.550	1.68	25.2	0.042	0.008	20.9	100.9	65.6	25	150
29_12	51.4	0.415	1.71	25.1	0.022	0.007	21.1	100.9	65.9	15	129
31_1	52.4	0.520	1.24	24.7	0.013	0.014	21.3	101.2	66.5	25	141
31_2	52.1	0.670	1.32	24.0	0.015	0.003	21.0	100.2	66.8	100	180
31_3	51.6	0.530	1.62	24.4	0.004	0.012	21.1	100.3	66.5	130	165
31_4	51.7	0.510	1.39	24.9	0.021	0.003	20.9	100.5	65.9	210	179
31_6	51.8	0.530	1.32	24.2	0.029	0.001	21.1	99.9	66.7	320	172
31_7	51.8	0.780	1.61	24.6	0.048	0.026	21.0	100.6	66.2	320	177
31_8	51.3	0.520	1.72	24.7	0.004	0.032	20.9	100.0	66.0	250	147
31_9	52.1	0.430	1.28	24.0	0.013	0.016	21.1	100.0	66.8	150	101
31_10	52.3	0.520	1.32	24.1	0.014	0.015	21.2	100.4	66.8	70	96
36_1	52.2	0.530	1.27	24.4	0.002	0.008	20.9	100.7	66.3	20	154
36_2	52.2	0.690	1.63	24.4	0.048	0.095	20.6	100.6	66.0	55	185
36_3	51.9	0.520	1.60	24.6	-0.029	0.001	20.5	100.3	65.7	180	184
36_4	51.2	0.620	1.43	25.2	0.034	0.002	20.5	100.1	65.1	170	185
36_5	51.2	0.610	1.64	24.9	0.062	0.029	20.7	100.2	65.6	150	163
36_6	51.6	0.550	1.66	24.3	0.028	0.022	21.3	100.6	66.8	90	154
36_7	51.5	0.510	1.56	24.2	0.026	0.006	20.7	99.6	66.3	65	142
36_8	52.2	0.640	1.27	24.5	0.036	0.020	21.0	100.8	66.3	15	135
40_1	51.3	0.910	1.62	25.4	0.020	0.002	20.5	100.6	65.0	30	180
40_2	51.3	0.890	1.51	25.4	0.023	0.018	20.4	100.4	64.9	70	175
40_3	51.2	0.920	1.45	24.8	b.d.	0.002	20.3	99.7	65.3	120	168
40_4	52.2	0.610	1.62	23.7	0.028	0.017	21.2	100.6	67.3	150	174
40_5	51.9	0.650	1.68	24.5	b.d.	0.003	20.3	100.1	65.6	180	189
40_6	52.4	0.550	1.67	24.4	b.d.	0.011	20.7	100.8	66.1	210	191
40_7	51.8	0.660	1.61	25.1	0.012	0.000	20.5	100.8	65.2	150	180
40_8	52.1	0.510	1.54	24.2	b.d.	0.012	21.2	100.7	66.8	90	165
40_9	51.5	0.680	1.43	25.8	0.035	0.026	20.7	101.0	64.8	60	135
47_1	51.6	0.620	1.35	24.3	b.d.	0.013	21.3	100.2	66.8	20	165
47_2	52.3	0.640	1.54	23.7	0.027	0.012	20.6	100.0	66.6	70	173
47_3	51.7	0.520	1.59	24.5	0.011	0.009	20.6	100.1	65.9	120	156
47_4	51.0	0.890	1.54	25.0	0.022	0.013	20.2	99.9	65.0	170	181
47_5	51.9	0.594	1.57	24.6	0.028	0.003	20.6	100.3	65.7	210	192
47_6	51.2	0.635	1.62	24.7	0.023	0.013	20.6	99.9	65.7	160	173
47_7	52.4	0.510	1.60	24.5	0.032	0.017	20.9	101.1	66.2	120	142
47_8	52.3	0.535	1.53	24.4	b.d.	0.014	20.5	100.3	65.9	80	135
47_9	52.1	0.538	1.57	24.6	0.026	0.016	20.8	100.7	66.0	30	113
50_1	51.6	0.565	1.76	24.8	b.d.	0.016	20.8	100.6	65.8	52	123
50_2	50.8	1.020	1.51	25.4	b.d.	0.024	20.9	100.4	65.4	70	220
50_3	50.7	0.940	1.61	25.5	b.d.	0.021	20.9	100.3	65.3	100	232
50_4	50.6	0.930	1.55	25.3	0.028	0.013	20.6	99.7	65.2	130	202
50_5	50.7	0.935	1.45	25.3	b.d.	0.026	20.7	99.8	65.3	160	232
50_6	50.8	0.925	1.50	25.4	0.017	0.012	21.0	100.3	65.5	210	260
50_7	50.7	0.930	1.43	25.2	0.002	0.012	21.1	100.1	65.8	210	272
50_8	50.9	0.920	1.59	25.3	b.d.	0.011	20.8	100.1	65.4	180	195
50_9	51.1	0.790	1.58	25.4	b.d.	0.015	20.9	100.4	65.4	130	195
50_10	50.9	1.030	1.62	25.9	0.017	0.010	20.7	100.8	64.7	80	208
50_11	50.7	1.050	1.63	24.6	0.030	0.012	20.7	99.3	65.9	50	151

50_11	50.7	1.050	1.63	24.6	0.030	0.012	20.7	99.3	65.9	50	151

	Na_2O	SiO_2	MgO	Al_2O_3	K_2O	CaO	TiO_2	Cr_2O_3	FeO	MnO	Total	Mg#
SSH_13_2	0.03	52.8	23.5	1.17	0	1.3	0.22	0.016	20.09	0.783	99.9	72.9
SSH_13_1	0.04	52.3	23.7	1.29	0	1.4	0.24	0	19.46	0.807	99.2	73.7
SSH_49_1	0.02	52.7	23.5	1.32	0	1.3	0.25	0.012	19.93	0.738	99.7	73.0
SSH_49_2	0.03	52.8	23.9	1.4	0	1.4	0.25	0.034	19.48	0.686	99.9	73.8
SSH_05_1	0.31	51.7	13.9	1.56	0.01	20.5	0.26	0	10.48	0.543	99.3	75.3
SSH_31_1	0.26	51.3	14.5	1.72	0.01	20.1	0.46	0	10.05	0.448	98.8	76.9
SSH_29_1	0.33	51.5	14.2	2.06	0	20.4	0.43	0	10.34	0.385	99.8	76.0
SSH_02_1	0.32	51.3	15.5	2.39	0	19.5	0.64	0	9.51	0.285	99.4	78.9
SSH_15_1	0.28	51.4	14.9	2.58	0	20.7	0.45	0	9.16	0.354	99.8	78.8
SSH_04_1	0.32	50.8	15.2	2.97	0	19.5	0.68	0.009	9.68	0.26	99.5	78.3

Pyr analysis	Melt H_2O, wt%	H_2O, ppm	Calculated Melt H_2O (using D=0.003)
SSH_01_01		3	0.1
SSH_02_01	0.003	2	0.1
SSH_05_1	1.5	89	3.0
SSH_04_1	0.06	18	0.6
SSH_08_01		130	4.3
SSH_09_01		160	5.3
SSH_12_01		14	0.5
SSH_13_01	5.06	159	5.3
SSH_15_01	4.35	281	9.4
SSH_15_02		164	5.5
SSH_17_01		153	5.1
SSH_18_01		52	1.7
SSH_20_01		139	4.6
SSH_23_01		20	0.7
SSH_24_01		103	3.4
SSH_25_01		119	4.0
SSH_26_01		75	2.5
SSH_27_01	0.01	87	2.9
SSH_29_1	5.62	178	5.9
SSH_30_01		158	5.3
SSH_31_01	0.01	156	5.2
SSH_32_01		188	6.3
SSH_35_01		67	2.2
SSH_45_01		213	7.1
SSH_46_01		141	4.7
SSH_47_01		159	5.3
SSH_49_01		165	5.5
SSH_49_02	6.19	230	7.7
SSH_49_3	0.03	71	2.4
SSH_49_4		55	1.8